8-2013

Radar Measurements of NHTSA's Surrogate Vehicle 'SS-V'

William Buller
Michigan Technological University

Brian Wilson
Michigan Technological University

James Ebling
Michigan Technological University

Line van Nieuwstadt
Michigan Technological University

Benjamin E. Hart
Michigan Technological University

U.S. Department
of Transportation
**National Highway
Traffic Safety
Administration**

NHTSA
www.nhtsa.gov

DOT HS 811 817

August 2013

Radar Measurements of NHTSA's Surrogate Vehicle SS_V

DISCLAIMER

This publication is distributed by the U.S. Department of Transportation, National Highway Traffic Safety Administration, in the interest of information exchange. The opinions, findings, and conclusions expressed in this publication are those of the authors and not necessarily those of the Department of Transportation or the National Highway Traffic Safety Administration. The United States Government assumes no liability for its contents or use thereof. If trade names, manufacturers' names, or specific products are mentioned, it is because they are considered essential to the object of the publication and should not be construed as an endorsement. The United States Government does not endorse products or manufacturers.

Technical Report Documentation Page

1. Report No.	2. Government Accession No.	3. Recipient's Catalog No.
DOT HS 811 817		

4. Title and Subtitle	5. Report Date
Radar Measurements of NHTSA's Surrogate Vehicle "SS_V"	August 2013
	6. Performing Organization Code NHTSA/NVS-312

7. Author(s)	8. Performing Organization Report No.
William Buller, Brian Wilson, James Ebling, Line van Nieuwstadt, and Benjamin Hart of the Michigan Tech Research Institute (MTRI) Sponsored/Monitored by Garrick Forkenbrock, National Highway Traffic Safety Administration	

9. Performing Organization Name and Address	10. Work Unit No. (TRAIS)
National Highway Traffic Safety Administration Vehicle Research and Test Center P.O. Box 37 East Liberty, OH 43319	11. Contract or Grant No.

12. Sponsoring Agency Name and Address	13. Type of Report and Period Covered
National Highway Traffic Safety Administration 1200 New Jersey Ave., S.E. Washington, D.C. 20590	Final Report
	14. Sponsoring Agency Code

15. Supplementary Notes.

16. Abstract

NHTSA seeks to objectively quantify the performance of forward-looking advanced technologies such as Crash Imminent Braking (CIB) and Dynamic Brake Support (DBS) on the test track. Since these evaluations are expected to result in collisions between the subject vehicle (SV) and a principal other vehicle (POV) positioned directly in front of it, safety necessitates that the POV be a surrogate. However, to insure the tests will provide an accurate assessment of the SV's CIB and/or DBS capabilities, the surrogate must present as realistic. One way "realism" must be quantified involves a surrogate's radar return characteristics.

The tests described in this report were performed to assess the radar return characteristics of NHTSA's Strikeable Surrogate Vehicle (SS_V), a test target visually similar to a small hatchback. This work was performed by Michigan Tech Research Institute (MTRI) and the University of Michigan's Transportation Research Institute (UMTRI) on August 5, 2012 and October 11, 2012 under US DOT/NHTSA contracts DTNH22-12-P-0158 and DTNH22-12-P-01638, respectively.

The tests performed indicate the SS_V is a viable surrogate for automotive safety tests where the SV approaches a POV from the tail-aspect.

17. Key Words	18. Distribution Statement
SS_V; Surrogate Vehicle; Advanced Technology, CIB, DBS, FCAM	Document is available to the public from the National Technical Information Service www.ntis.gov

19. Security Classif. (of this report)	20. Security Classif. (of this page)	21. No. of Pages	22. Price
Unclassified	Unclassified	115	

Form DOT F 1700.7 (8-72) Reproduction of completed page authorized

Contents

List of Tables

Acknowledgements

The evaluation of the National Highway Traffic Safety Administration (NHTSA) surrogate targets is made possible by funding provided by NHTSA for the collection and analysis of the SS extunderscoreV1 and SS_V2, as well as, a representative vehicle. The analysis in the report makes use of additional measurements, a library of 26 vehicles, performed with the sponsorship and assistance of Toyotas Collaborative Safety Research Center (CSRC) in Ann Arbor, Michigan. All the measurements collected for this study are aided by the employees and facilities at the University of Michigan's Transportation Research Institute (UMTRI). The authors are very grateful for the contributions and support of Garrick Forkenbrock (NHTSA), Rini Sherony (CSRC), Dave LeBlanc (UMTRI) and Mark Gilbert (UMTRI).

1 Executive Summary

This report covers the collection and analysis of NHTSA's test surrogate SS_V, on August 5, 2012, conducted under Order DTNH22-12-P-0158 and on October 11, 2012, conducted under Order DTNH22-12-P-01638. This report is comprehensive with analysis of measurements made by Michigan Tech Research Institute (MTRI) and the University of Michigan's Transportation Research Institute (UMTRI). This program is sponsored by the Vehicle Research and Test Center, US DOT/NHTSA.

Throughout this report the target sampled on August 5, 2012 is referred to as SS_V1. Based in part on recommendations provided by MTRI, NHTSA modified its surrogate design and made possible a second collection to analyze the results. The modified surrogate sampled on October 11, 2012 is referred to as SS_V2.

The SS_V1 and SS_V2 are intended as surrogate targets, substitutes for actual vehicles, in safety tests to evaluate the performance of collision mitigation systems. To characterize the performance of collision mitigation systems, the surrogate should *behave* like a vehicle would behave to the mitigation system. We've measured the reflectance of the surrogates with a W and Ka band radar to evaluate the surrogates' behavior.

The radar cross-section (RCS) of any target may be considered as a random variable drawn from a statistical distribution. The detection and tracking functions performed by the radar are impacted by the statistical distribution of the RCS and the nature of the fluctuations (i.e. how the distribution is sampled). For this reason we consider three figures of merit:

> The instability of the target as defined by equation 1. Surrogates with high instability measurement, ϵ, cannot be expected to accurately predict the detection and tracking performance of the radar under test.
>
> $$\epsilon = \langle \frac{\Delta\sigma(f)}{\sigma(f)} \rangle_f \tag{1}$$
>
> The expected value of the radar cross section, as expressed in 2. The expected RCS of the target provides a sense of how large the target's reflected power will appear to the radar.
>
> $$\overline{\sigma} = \langle \sigma(f,\theta) \rangle_{f,\theta} \tag{2}$$

The best-fit Weibull parameters for the radar cross-section, as expressed in 3

$$P_W(\sigma(\theta, f); \alpha, \beta) = \alpha\beta^{-\alpha}\sigma^{\alpha-1}e^{-(\frac{\sigma}{\beta})^{\alpha}} \quad (3)$$

To help quantify the impact on safety tests, we evaluate how performance estimates using the surrogate compare to performance estimates using a car in automotive safety tests. We compute the figures of merit for the surrogate target and compare them to the Vehicle Domain (excluding the motorcycle). Further, we define a *Nominal Vehicle* as one whose Weibull parameters lie in the middle of the Vehicle Domain for all of the sampled vehicles. The surrogate is considered vehicle-like if it is within the Vehicle Domain. The Nominal Vehicle is defined as a fiduciary for comparing performance estimates, discussed in more detail following.

The SS_V1 and SS_V2 are rigid body targets that do not fluctuate with repeated measurements. The instability metric, , shows this in Table 1. The SS_V1 and SS_V2 share a flat strike-plate area that produces a strong specular response. The SS_V1, additionally had a specular response from its rear window that was excessive compared to that observed from vehicles. Measurements in the field showed that the rear glass is semi-transparent at Ka band. Both targets are within the domain of vehicle signatures at W-band and exceed the expected RCS, $\overline{\sigma}$, at Ka-band; although, the amount is negligible in the case of the SS_V2.

Thus, the SS_V2 appears to a W or Ka-band radar approaching its tail-aspect, 180°, as a strongly reflecting vehicle. We consider estimating the errors incurred by a hypothesis test deciding whether a car is there or not, and compare the performance of the SS_V2 with the Nominal Vehicle.

It is important to remember that the discrepancy between the DET plots for the SS_V2 and the Nominal Vehicle should not be interpreted as errors - actual vehicles will also differ from the Nominal Vehicle. What we discover, by inspection of the detector error trade-off (DET) plot in Figure 1, is that the Nominal Vehicle is likely to incur a higher error rate; or, said another way, the SS_V2 will provide *optimistic* performance estimates compared to the Nominal Vehicle. This is also true for many actual vehicles. By similar analysis, it is shown in Section 8.3, that the SS_V2 provides *pessimistic* performance estimates as the approach vehicle views the target at aspects away from 180.0°

Table 1: Evaluation of SS_V1 and SS_V2 by three figures of merit using the tail aspect, 180 °

Band	Target	(unitless)	$\overline{\sigma}$ (dBm^2)	Weibull α, β (m^2)
W	Vehicle Domain	< 0.07	4-22	0.5-1.3, 2-160
W	NHTSA SS_V1	0.04	15	1.0, 32
W	NHTSA SS_V2	0.03	21	1.1, 126
Ka	Vehicle Domain	< 0.02	13-17	1-1.2, 20-50
Ka	NHTSA SS_V1	0.004	21	1.0,126
Ka	NHTSA SS_V2	0.007	18	1.1, 63

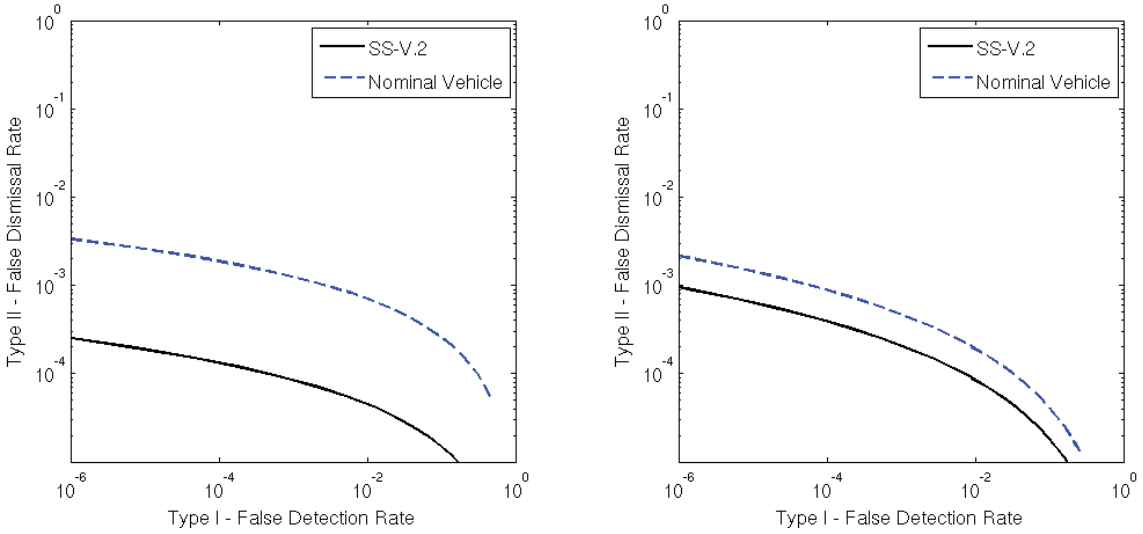

(a) W-band errors.

(b) Ka-band errors.

Figure 1: Comparison of errors expected for detection of the SS_V2 and a Nominal Vehicle in road conditions when viewing is restricted to tail aspect.

2 Introduction

With the ultimate goal of preventing, or mitigating vehicle collisions, auto makers are developing and offering Pre-Collision Systems (PCS) capable of automatically applying or supplementing the driver's brake inputs in some of their vehicle models. The subject of this paper is the evaluation of surrogate targets for testing automotive PCS units. The primary challenge to realizing a PCS evaluation test set-up lies with the ill-defined nature of the target and clutter; specifically, how would automobiles with their various shapes and sizes be distinguished from the variety of road objects and other hazards.

Vehicle crashes that are applicable to mitigation through a PCS include rear-end collision, object crashes and collision with opposing traffic. Of these, rear-end collisions comprise the majority [1], based on National Automotive Sampling System/Crashworthiness Data System (NASS/CDS) from years 1997 to 2008 [2]. Of the three million vehicles involved in PCS applicable crashes, 1.9 million were rear-end collisions. Of these rear-end collisions, more than 22 thousand occupants suffered serious injury and nearly 3 *thousand* suffered fatalities.

The key to reducing collision injury is to foresee collisions as soon as possible and to pre-emptively activate safety devices to increase their effectiveness. Until now, safety systems were made to activate only after a collision occurred. Activating them in advance requires that an unavoidable collision be anticipated. The newly developed PCS make it possible to predict a collision and activate safety devices ahead of an impact.

Based on crash frequency, cost and harm data [3], NHTSA has developed test procedures to emulate real world crash scenarios to evaluate the performance of forward crash warning systems. Similar considerations motivate the test procedure for PCS, in general. Principal among these considerations is that the most important scenarios involve a lead vehicle stopped, decelerating or moving at a slower speed, with the striking vehicle approaching from the rear. This motivates the collection of radar reflectance data from the rear aspects of the vehicles.

We have measured, calibrated and analyzed the radar signatures of a test vehicle and test surrogate consistent with the collection procedure used previously to assess a set of 26 vehicles. The vehicle and surrogate are measured at W-band (90-98 GHz) and a subset of these are analyzed at Ka-band (26.5-36.5 GHz). Radar signatures are collected at viewing angles consistent with those expected for a pre-collision system. The target vehicles are viewed at

180.0, 182.5 and 185.0 degrees, where aspect 180° is tail-on. The viewing angle is varied from each aspect over an additional 3 degrees variation in azimuth. The entire set of angles is then collected with the radar elevated at 1.5°

Range-profiles and real beam imagery have been analyzed to understand the vehicle elements that contribute the most significantly to the radar signature. This allows for an understanding of the strength and spatial separation of scattering sources. The signatures of the vehicles have been fit to a Weibull distribution to understand the variation in the signatures. The performance of a radar's detection and tracking functions are predictable if the target and clutter distributions can be characterized.

3 Vehicle Selection

We have selected popular vehicle models from within the nine most common vehicle types struck in rear end crashes. The vehicle types and specific models representating struck vehicles are based on an analysis of light vehicle-striking crashes from the U.S. Department of Transportation's General Estimates System (GES) [2].

Table 2: Vehicles selected for measurements at W-band and rank among vehicles struck in rear-end collisions. Some models are not ranked in the GES. Vehicles that are marked in **bold** were also measured at Ka-band.

Table Make/Model	Year	Rank
Full-Size Chevy Pickup	2005	2
Honda Accord	**2007**	**3**
Toyota Camry	2004	5
Ford Taurus 500	2007	8
Toyota Corolla	2009	9
Honda Civic	2010	12
Full-Size GMC Pickup	**2001**	**13**
Nissan Altima	2003	15
Chevrolet Impala	2010	16
Toyota Tacoma 4WD	2002	18
Chevrolet Suburban	**2009**	**21**
Toyota RAV4	**2008**	**35**
Jeep Patriot	2010	36
Toyota Sienna	2008	54
GMC Savana	2010	63
Toyota Matrix	2009	196
Nissan 360Z	2005	197
Scion xB	2008	264
Subaru Outback	2005	288
Toyota Prius	2010	300
Toyota Yaris	2010	-
Honda Fit	**2009**	**-**
Chrysler 200	2011	-
GMC Acadia	2007	-
Honda Nighthawk 750	1993	-
Ford Fiesta Hatchback	**2011**	**-**

4 Measurement Methods

4.1 Collection Geometry

The MTRI instrumentation radars use lens antennas that produce nominal 1.5° beamwidth, achieving a gain of 43 dB. The radars scan the vehicles at

several azimuths, elevations and aspect angles. A linear translation stage, shown in Figure 2, was constructed that transports the antenna upto 3.5 meters. The antenna head is set on a tilt-pan platform. The targets are viewed from a standoff of approximately 40 meters. At this standoff range, the beamspot is approximately 1 meter in diameter.

Figure 2: The W-band head is shown on the translation stage. A technician verifies the azimuth and elevation of the pan-tilt head.

Targets are scanned at 30 angles: 3 aspects, 2 elevations and 5 azimuths. Aspect angles of 180.0°, 182.5° and 185.0°, measured from target vehicle's nose vector, as shown in Fig. 3, are sampled by translating the antenna head in cross-range by 0, 1.75 and 3.5 meters. The elevation is set in turns to 0.0° and 1.5° The range profiles are plotted in Cartesian coordinates to create real-beam images.

The various angle and frequency measurements are used to generate a probability density function of the measured radar cross-sections. The same measurement procedure is used to evaluate surrogate test targets. The wide-

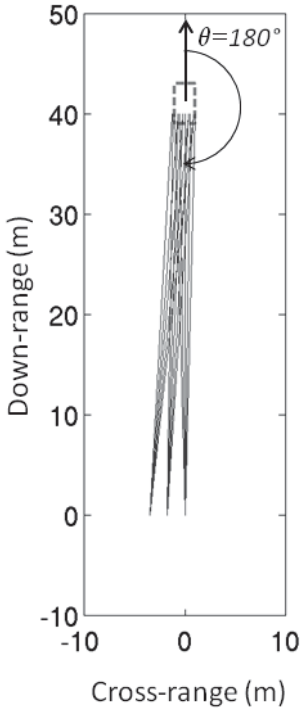

Figure 3: Radar is translated in cross-range to obtain measured data from near tail aspects: 180°, 182.5°, 185° The plot is projected into the *x-y plane* Measurements were made at 0.0° and 1.5° in elevation.

band response of the vehicles, viewed at multiple rear-aspects, is analyzed statistically A wideband radar-cross section (RCS), to provide a robust metric [4], is used to characterize the scattering.

The measurements here are not typical RCS target models, as the statistic is developed from sparse sampling in angle and over a wideband. However, they do serve two purposes: 1.) to understand RF reflections from many vehicles and 2.) to develop an RCS statistic that may be used to evaluate surrogate targets. Details of the statistical modeling of these vehicles are presented in [5].

The fluctuation model developed for the targets in our test is valid for the sampling with this collection geometry The fluctuation model for a vehicle at rear aspect during a crash scenario, would be populated by a dense sampling

of radar reflections from a smaller angular extent and a larger domain of range.

4.2 Collection Bands

Typical automobile PCS employ radars, lidars and cameras to predict collisions. Current automotive radars operate at W-band (77 GHz) and Ka-band (24 GHz). Collection bands are selected that have similar wavelengths to mimic the radar response; however, MTRI is using existing instrumentation radars with high-resolution waveforms. The MTRI W-band radar samples from 90 to 98 GHz and the Ka-band radar samples from 26.5 to 34.5 GHz. Thus, both radar transceivers are collecting 8 GHz of bandwidth. In both cases, the wide bandwidth allows us to resolve target scattering to within 2 centimeters. This is neither typical nor advisable for use in automotive PCS, but allows us to identify sources of scattering with much greater detail than a radar intended for detection and tracking functions. The MTRI radars transmit up to 200 milliwatts of power. As with automotive radars, the transmissions are linearly polarized, and the transmit and receive antennas are aligned for co-polarized reception. These parameters are summarized in 3. The wiring diagram for instrument is also provided in 4.

Table 3: Radar parameters for 2011-2012 automotive radar cross-section collections by MTRI

Parameter	W-band Spec	Ka-band Spec
Mode of Operation	Stepped-CW	Stepped-CW
Center Frequency	94 GHz	30.5 GHz
Bandwidth	8 GHz	8 GHz
Transmitted Power	200 mW	200 mW
Polarization	H-H	H-H
Waveform Repetition Freq	3 Hz	3 Hz

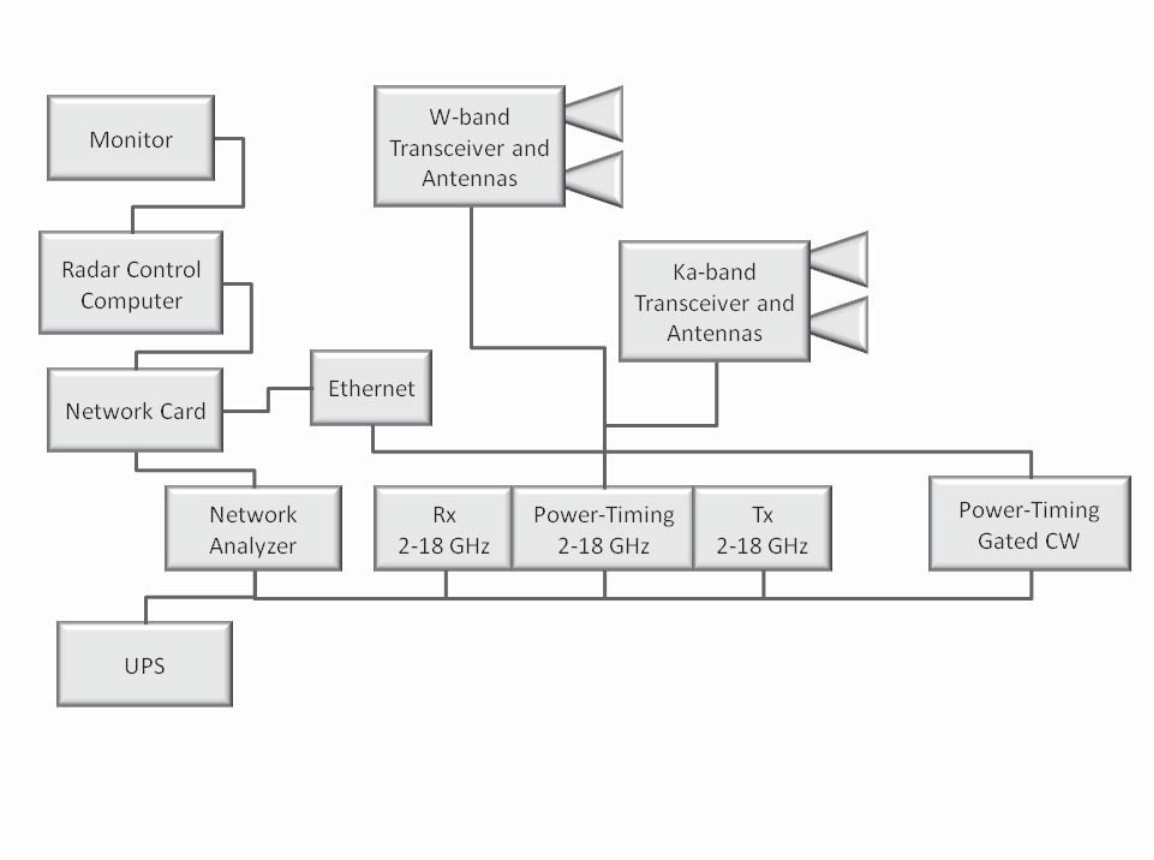

Figure 4: The schematic of the MTRI Instrumentation Radar with both W and Ka band heads.

4.3 Calibration

The data is calibrated to convert the power measured at the receiving antenna into an estimate of the radar cross-section (RCS) of the target. This is achieved by measuring a target with a known RCS. In the case of this study, MTRI used a triangular corner cube with edge measurement, a, equal to 7 centimeters. The calibration target is attached to tripod and a radar absorbing tile is set to help obscure the tripod and mitigate ground reflections.

Figure 5: The trihedral corner reflector used for calibration.

A triangular corner cube has a theoretical value as expressed in equation 4.

$$\sigma(\lambda) = \frac{4\pi a^4}{3\lambda^2} \tag{4}$$

The received power, P_{Rx}, is related to the RCS of the target, σ, [6] through the equation 5, where the transmit and receive gain of the antenna are G_{Tx},

G_{Rx}, respectively

$$P_{Rx} = P_{Tx}\frac{G_{Tx}G_{Rx}}{(4\pi)^3}^2\frac{\sigma}{R^4} \tag{5}$$

At each wavelength, we can express the received power as in equation 6.

$$P_{Rx} = \kappa\frac{\sigma}{R^4} \tag{6}$$

Measuring a target with known RCS, σ_0, we can solve, in 8, for the coefficient of calibration, κ

$$\kappa(\ ) = \frac{P_{Rx}R^4}{\sigma_0(\ )} \tag{7}$$

Re-arranging equation 8 allows us to convert received power into measured RCS, σ_M

$$\sigma_M(\ ) = \frac{P_{Rx}R^4}{\kappa(\ )} \tag{8}$$

5 Radar Cross-Section Measurements

5.1 Representative Vehicle Reflectance at W-Band

The NHTSA surrogate is compared to a 2011 Ford Fiesta Hatchback, shown in Figure 6. The vehicle's side view, Figure 7 is important to understand, as radar returns are plotted as a function of range. The Fiesta is 4.064 meters in length. The MTRI W-band radar scans 8 GHz of bandwidth and has a resolution of approximately 2 cm. Overlaying plots of the radar returns on a scaled side-view image of the vehicle allows us to better understand the source of significant radar reflections. Overlay plots are shown for horizontal viewing of the target and when the radar is aimed up in elevation by 1.5°, Figure 8.

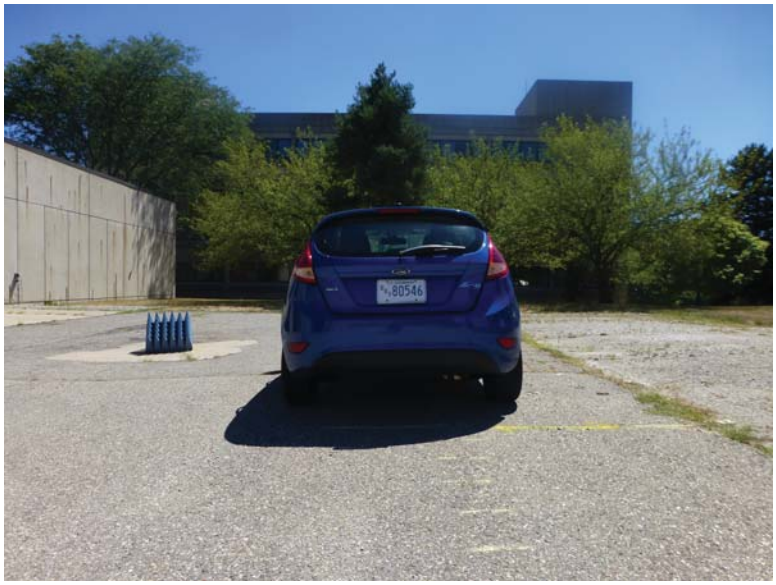

Figure 6: Ford Fiesta - Rear View

Figure 7: Ford Fiesta - Side View

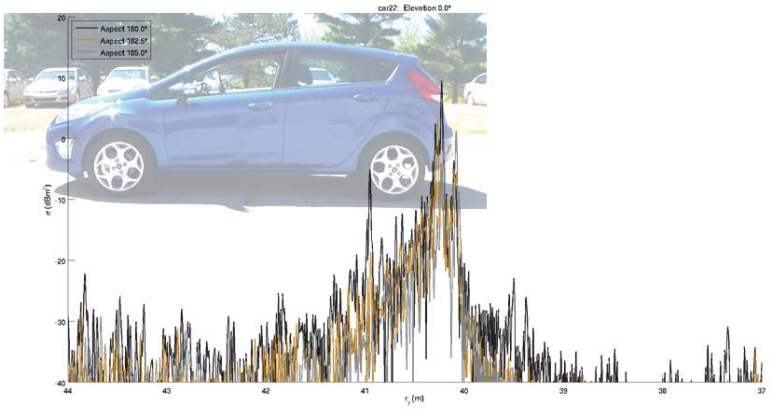

(a) Ford Fiesta (2011) returns at 0.0° in elevation

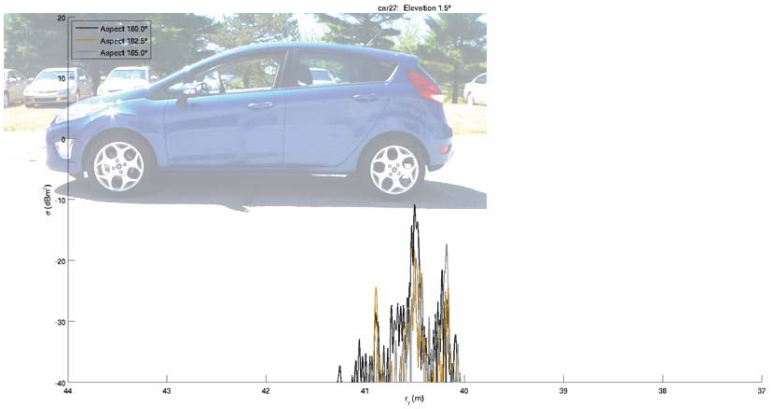

(b) Ford Fiesta (2011) returns at 1.5° in elevation

Figure 8: W-band range profiles of 2011 Ford Fiesta Hatchback overlaid on vehicle image scaled to plot. The range profiles are collected at an elevation of 0.0° and 1.5° and azimuths of 180.0° (black), 182.5° (gold) and 185.0° (silver).

5.2 Representative Vehicle Reflectance at Ka-Band

The MTRI Ka-band radar also scans 8 GHz of bandwidth and has a resolution of approximately 2 cm. Overlaying plots of the radar returns on a scaled side-view image of the vehicle allows us to better understand the source of significant radar reflections. Radar returns at Ka-band are shown for horizontal viewing of the target and when the radar is aimed up in elevation by 1.0°, Figure 9. The Ka-band collections on August 5, 2012 were made at 1.0° in elevation rather than 1.5° in elevation

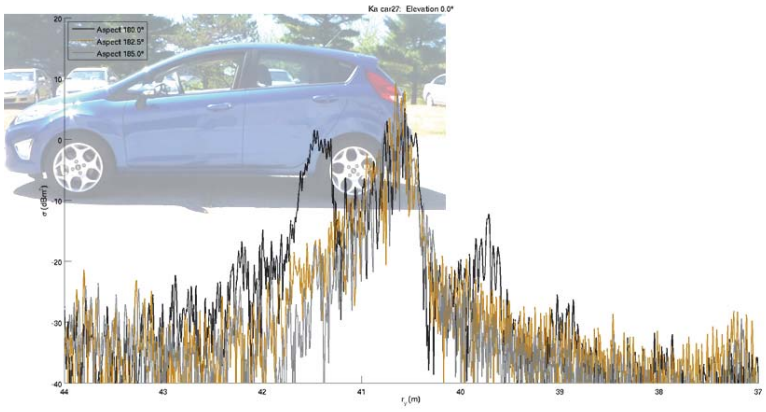

(a) Ford Fiesta (2011) returns at 0.0° in elevation

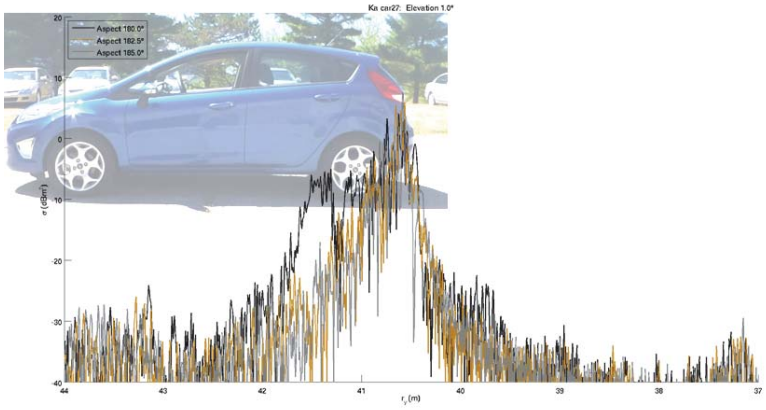

(b) Ford Fiesta (2011) returns at 1.0° in elevation

Figure 9: Ka-band range profiles of 2011 Ford Fiesta Hatchback overlaid on vehicle image scaled to plot. The range profiles are collected at an elevation of 0.0° and 1.0° and azimuths of 180.0° (black), 182.5° (gold) and 185.0° (silver).

5.3 Reflectance of Selected Vehicles at W-band

In work conducted with Toyota Collaborative Safety Research Center and University of Michigan's Transportation Research Institute, MTRI assayed 25 vehicles at W-band and 5 were selected for scanning at Ka-band. In this section the central azimuth sweep from three aspects is plotted over the scaled image of the vehicles to show the radar reflectance and provide spatial information about the returns. The central azimuth sweep at 180.0° is plotted in black; the central azimuth sweep at 182.5° is plotted in gold; and the central azimuth sweep at 185.0° is plotted in silver. There are two images with overlay data for each vehicle. One is collected with the radar pointed horizontally at approximately bumper height (45 cm). The second is collected with the radar pointed up at 1.5° elevation, which at the range of 40 meters is approximately centered at 1.95 meters above the ground. This provides isolation of scattering due to chassis components and upper-body components. The overlay data help show the process by which researchers in the field, with measuring tapes, used the radar range profiles to identify sources of scattering from the chassis and upper-body Significantly, scattering typically originates with reflections from the bumper, the license plate shelter, tail-lights, muffler, rear-axle, differential and chassis supports. Field notes, range profiles and real-beam images formed from the full collection of data were used to identify principal scattering sources, their relative locations, separations and sizes. This section, covers pages 23 through 47, provides a comprehensive overview of the radar returns for twenty-five vehicles.

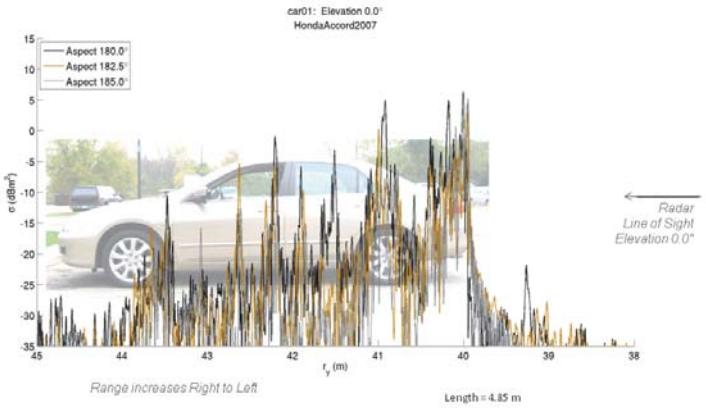

(a) Honda Accord (2007) returns at 0.0° in elevation

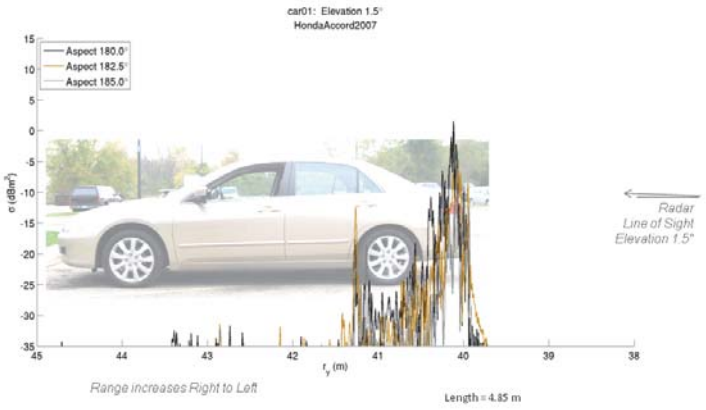

(b) Honda Accord (2007) returns at 1.5° in elevation

Figure 10: Honda Accord (2007) W-band radar returns at center azimuth, for each aspect, overlaying scaled vehicle image.

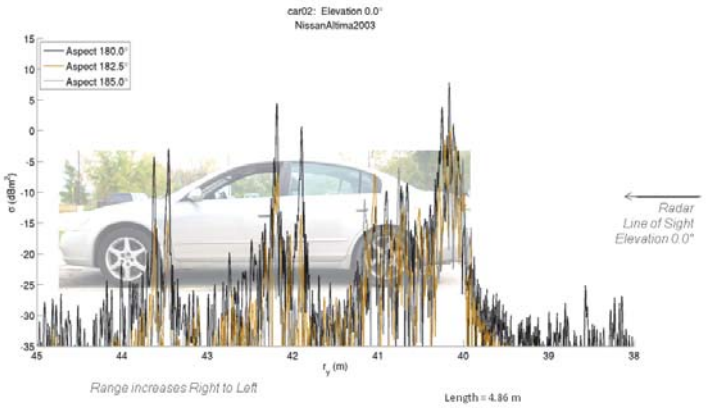

(a) Nissan Altima (2003) returns at 0.0° in elevation

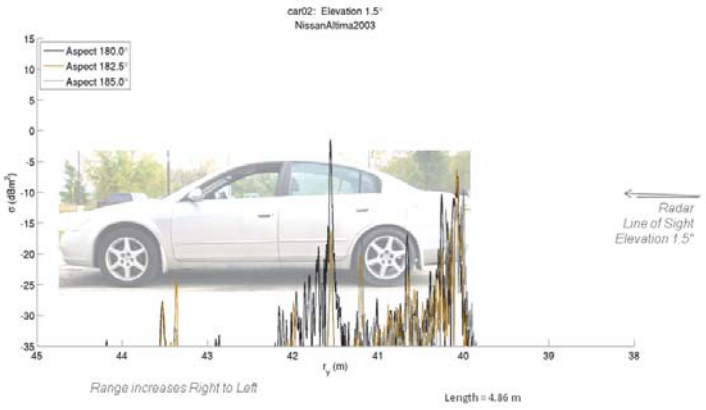

(b) Nissan Altima (2003) returns at 1.5° in elevation

Figure 11: Nissan Altima (2003) W-band radar returns at center azimuth, for each aspect, overlaying scaled vehicle image.

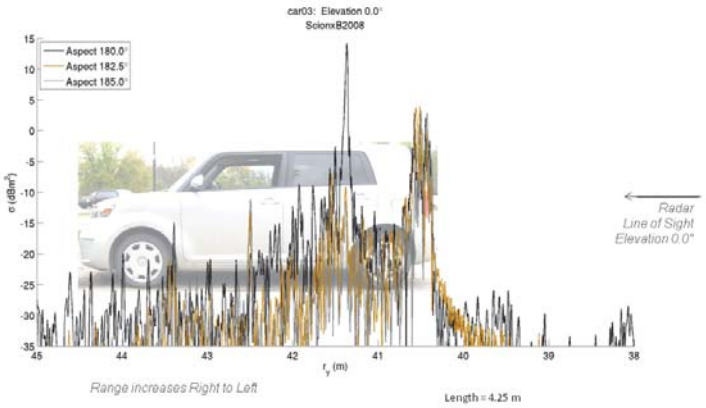

(a) Scion xB (2008) returns at 0.0° in elevation

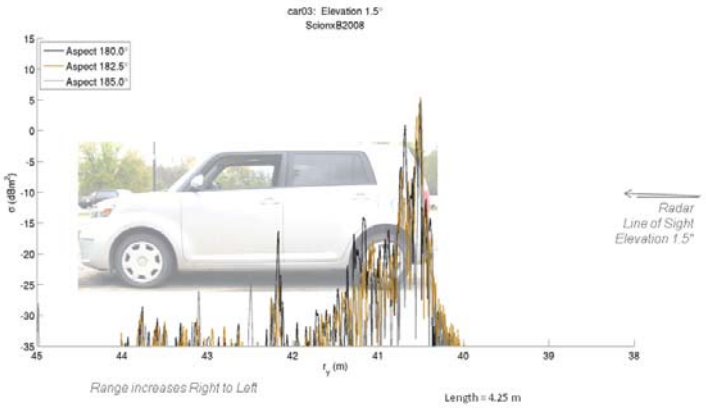

(b) Scion xB (2008) returns at 1.5° in elevation

Figure 12: Scion xB (2008) W-band radar returns at center azimuth, for each aspect, overlaying scaled vehicle image.

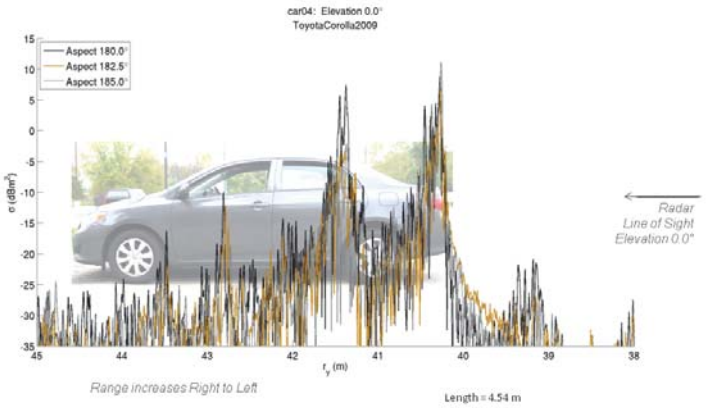

(a) Toyota Corolla (2009) returns at 0.0° in elevation

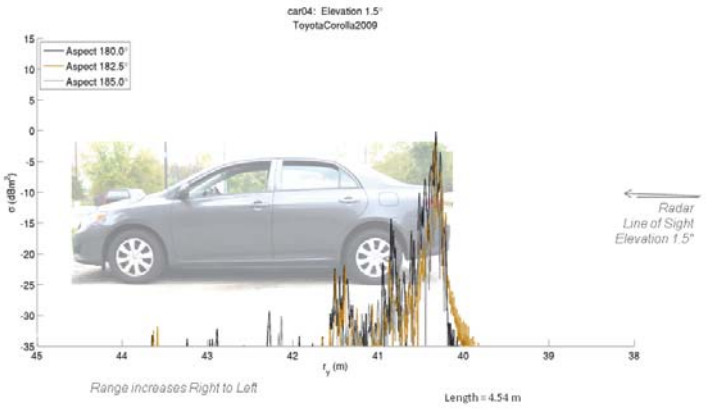

(b) Toyota Corolla (2009) returns at 0.0° in elevation

Figure 13: Toyota Corolla (2009) W-band radar returns at center azimuth, for each aspect, overlaying scaled vehicle image.

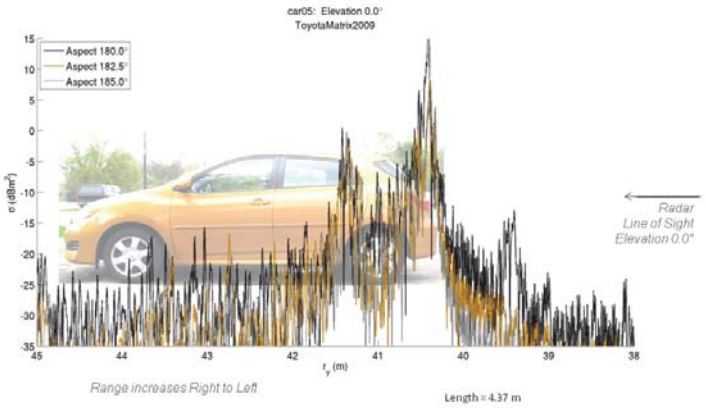

(a) Toyota Matrix (2009) returns at 0.0° in elevation

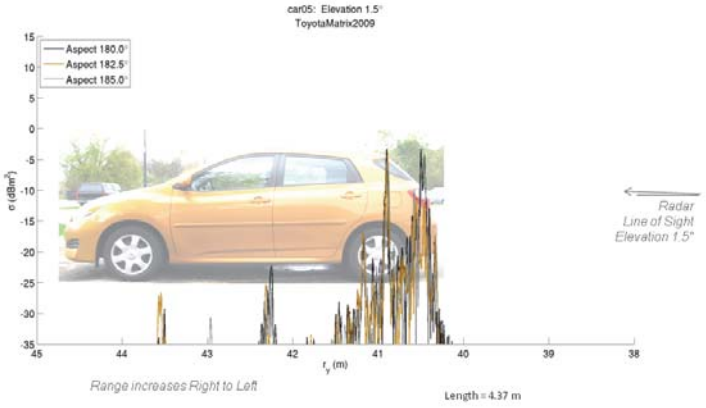

(b) Toyota Matrix (2009) returns at 1.5° in elevation

Figure 14: Toyota Matrix (2009) W-band radar returns at center azimuth, for each aspect, overlaying scaled vehicle image.

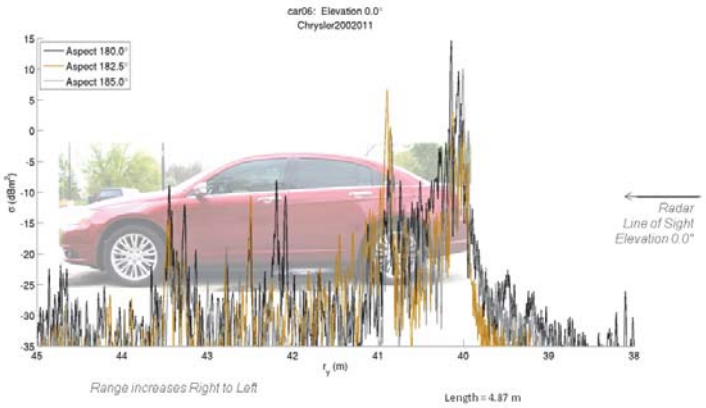

(a) Chrysler 200 (2011) returns at 0.0° in elevation

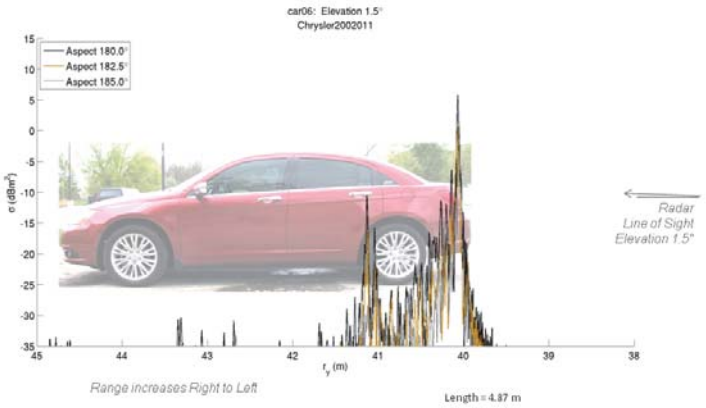

(b) Chrysler 200 (2011) returns at 1.5° in elevation

Figure 15: Chrysler 200 (2011) W-band radar returns at center azimuth, for each aspect, overlaying scaled vehicle image.

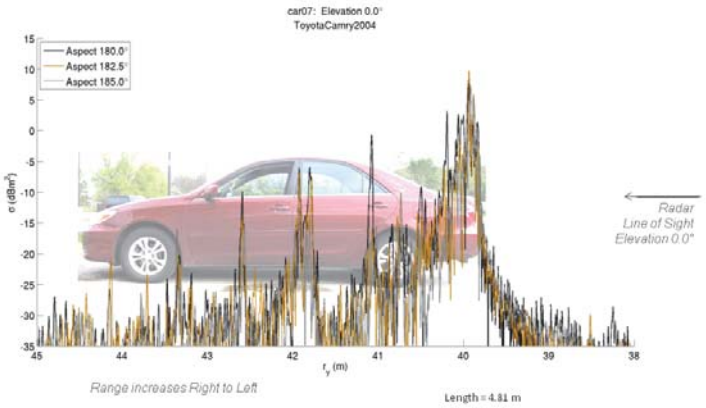

(a) Toyota Camry (2004) returns at 0.0° in elevation

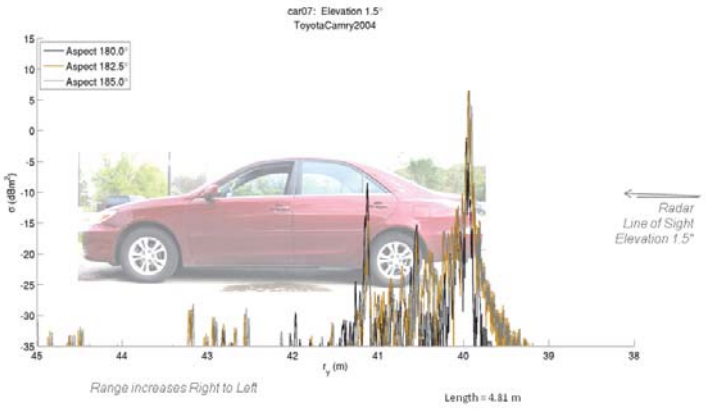

(b) Toyota Camry (2004) returns at 1.5° in elevation

Figure 16: Toyota Camry (2004) W-band radar returns at center azimuth, for each aspect, overlaying scaled vehicle image.

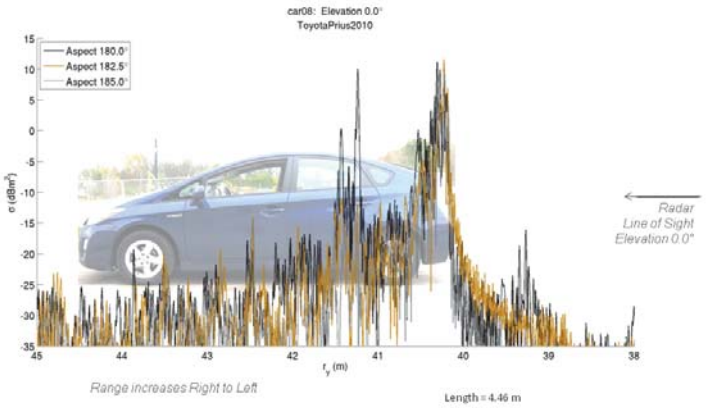

(a) Toyota Prius (2010) returns at 0.0° in elevation

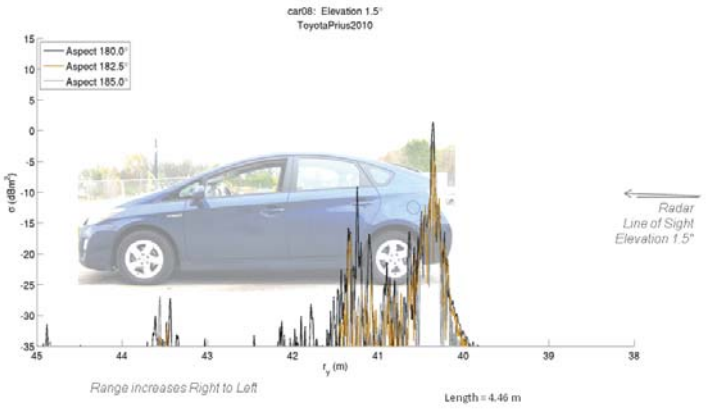

(b) Toyota Prius (2010) returns at 1.5° in elevation

Figure 17: Toyota Prius (2010) W-band radar returns at center azimuth, for each aspect, overlaying scaled vehicle image.

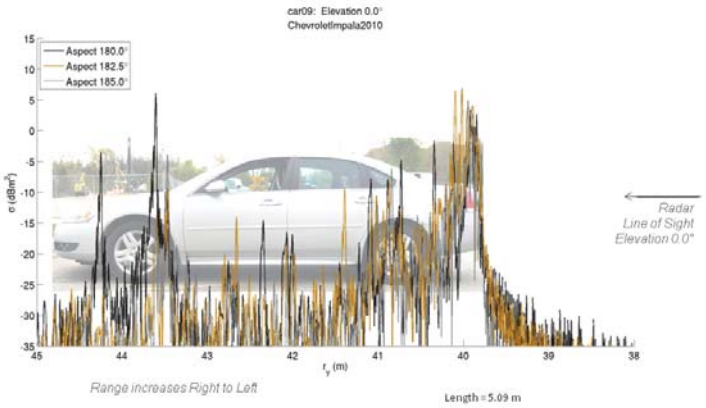

(a) Chevrolet Impala (2010) returns at 0.0° in elevation

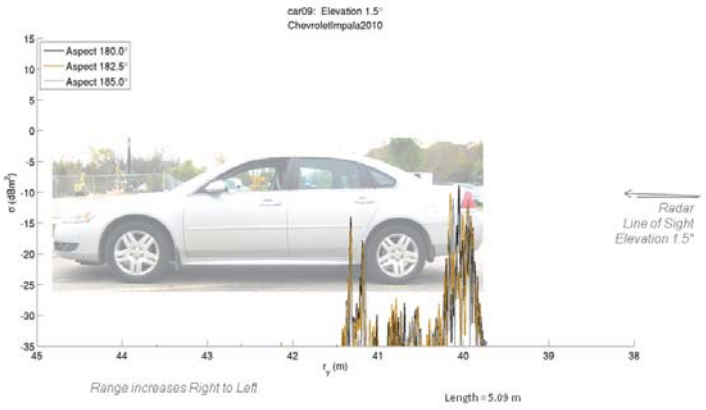

(b) Chevrolet Impala (2010) returns at 1.5° in elevation

Figure 18: Chevrolet Impala (2010) W-band radar returns at center azimuth, for each aspect, overlaying scaled vehicle image.

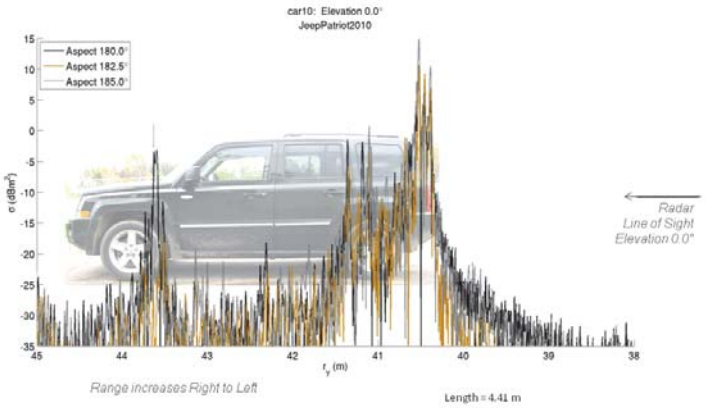

(a) Jeep Patriot (2010) returns at 0.0° in elevation

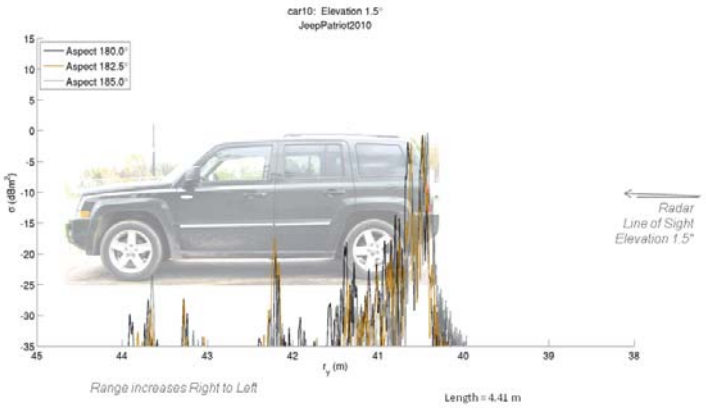

(b) Jeep Patriot (2010) returns at 1.5° in elevation

Figure 19: Jeep Patriot (2010) W-band radar returns at center azimuth, for each aspect, overlaying scaled vehicle image.

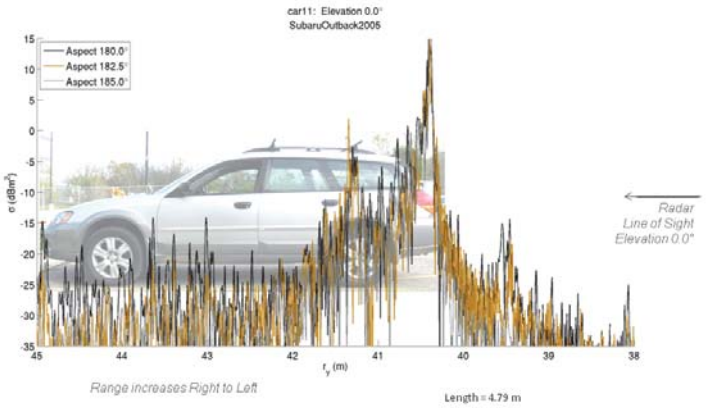

(a) Subaru Outback (2005) returns at 0.0° in elevation

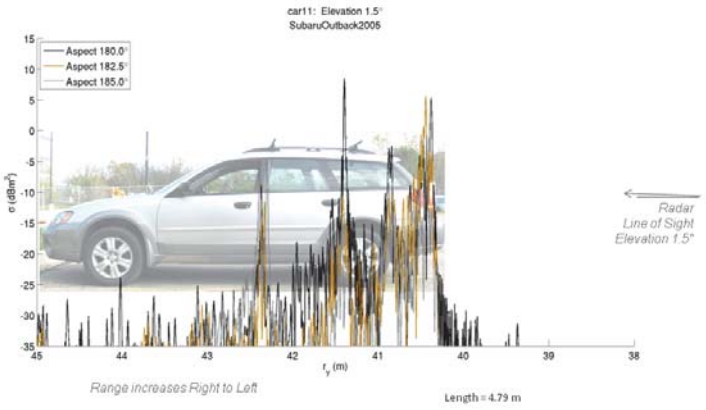

(b) Subaru Outback (2005) returns at 1.5° in elevation

Figure 20: Subaru Outback (2005) W-band radar returns at center azimuth, for each aspect, overlaying scaled vehicle image.

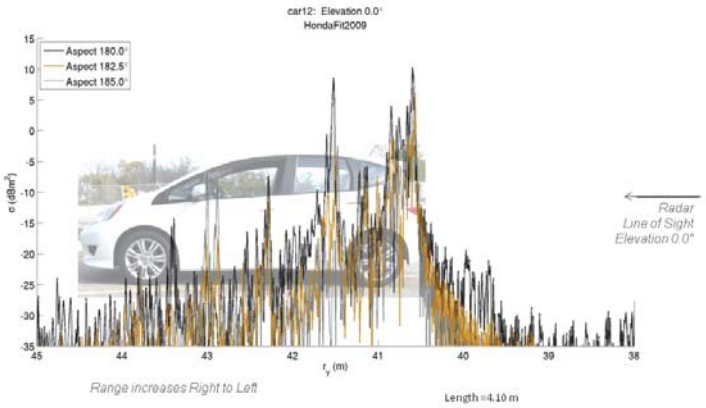

(a) Honda Fit (2009) returns at 0.0° in elevation

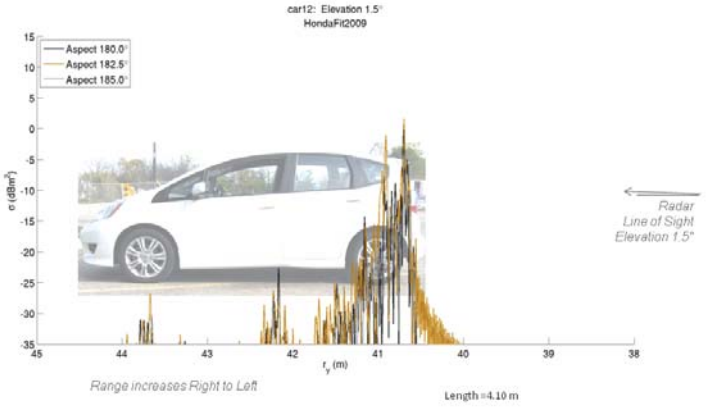

(b) Honda Fit (2009) returns at 1.5° in elevation

Figure 21: Honda Fit (2009) W-band radar returns at center azimuth, for each aspect, overlaying scaled vehicle image.

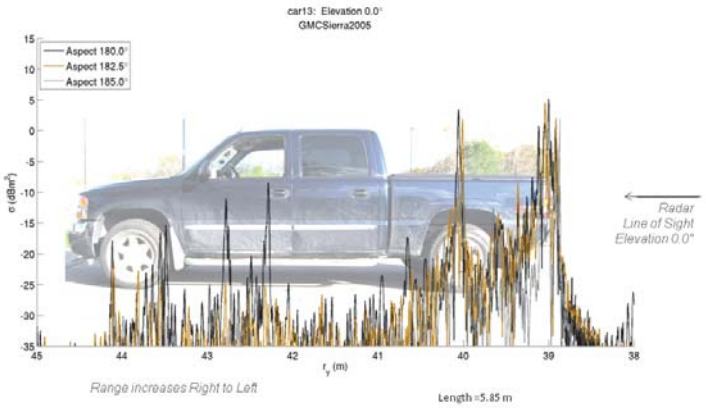

(a) GMC Sierra (2005) returns at 0.0° in elevation

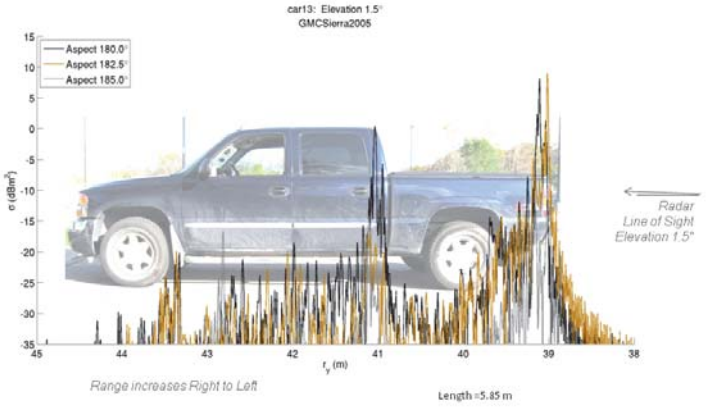

(b) GMC Sierra (2005) returns at 1.5° in elevation

Figure 22: GMC Sierra (2005) W-band radar returns at center azimuth, for each aspect, overlaying scaled vehicle image.

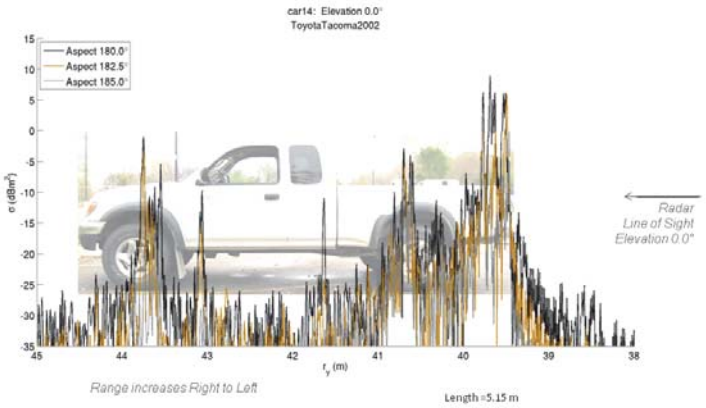

(a) Toyota Tacoma (2002) returns at 0.0° in elevation

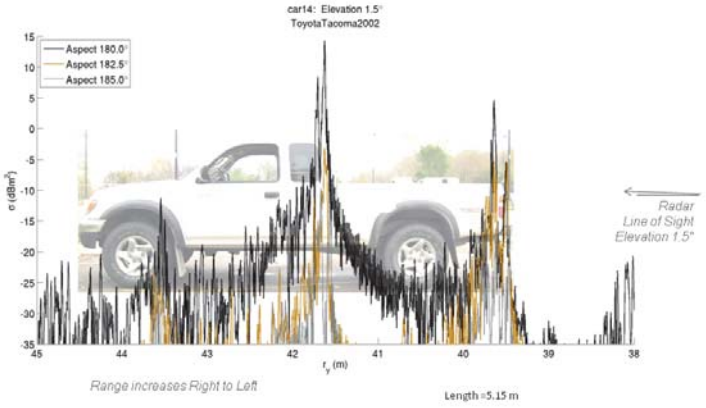

(b) Toyota Tacoma (2002) returns at 1.5° in elevation

Figure 23: Toyota Tacoma (2002) W-band radar returns at center azimuth, for each aspect, overlaying scaled vehicle image.

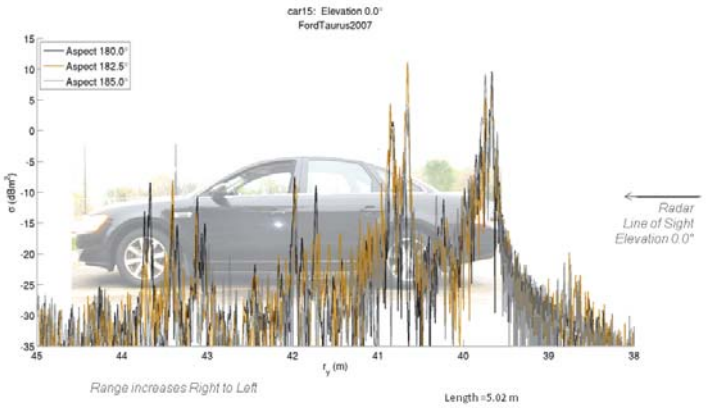

(a) Ford Taurus (2007) returns at 0.0° in elevation

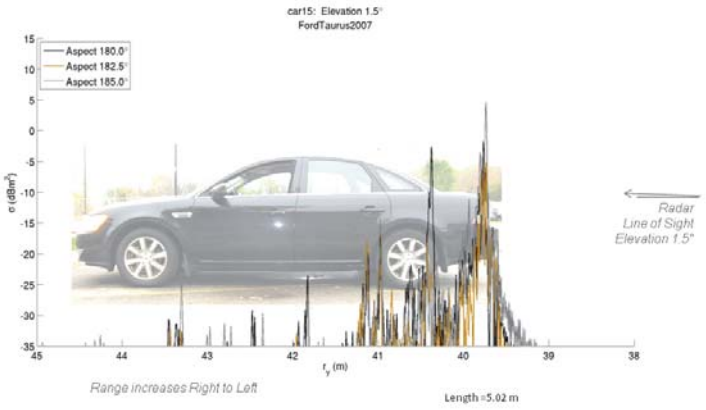

(b) Ford Taurus (2007) returns at 1.5° in elevation

Figure 24: Ford Taurus (2007) W-band radar returns at center azimuth, for each aspect, overlaying scaled vehicle image.

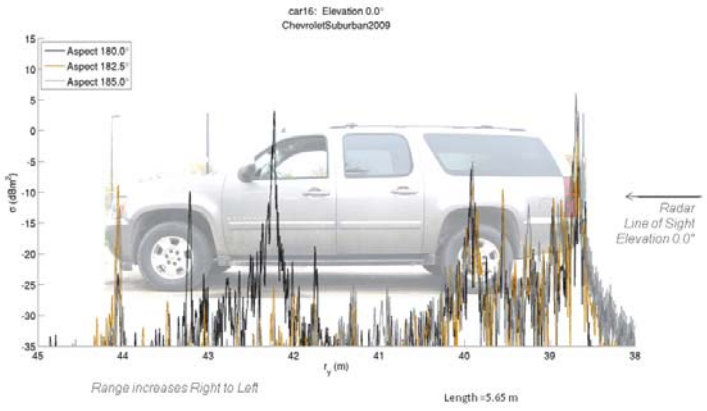

(a) Chevrolet Suburban (2009) returns at 0.0° in elevation

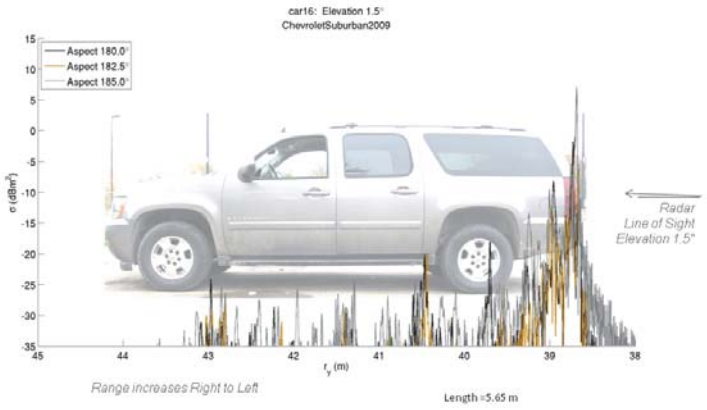

(b) Chevrolet Suburban (2009) returns at 1.5° in elevation

Figure 25: Chevrolet Suburban (2009) W-band radar returns at center azimuth, for each aspect, overlaying scaled vehicle image.

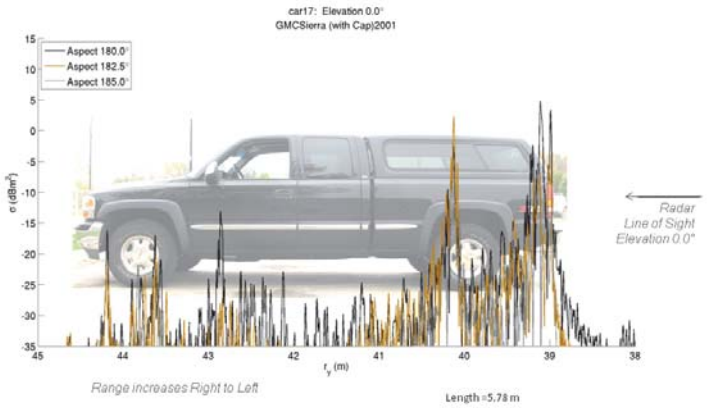

(a) GMC Sierra with Cap (2001) returns at 0.0° in elevation

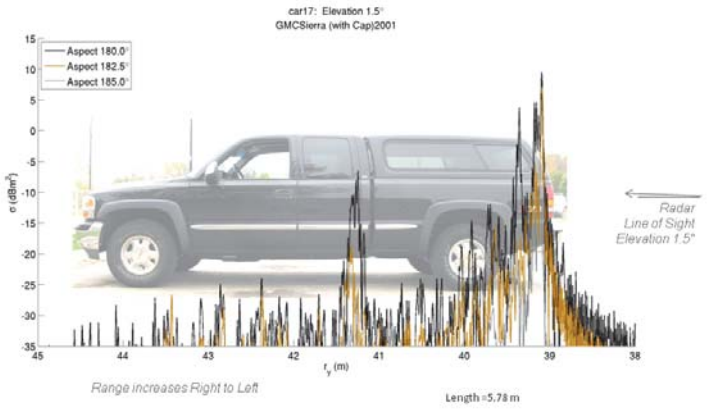

(b) GMC Sierra with Cap (2001) returns at 1.5° in elevation

Figure 26: GMC Sierra with Cap (2001) W-band radar returns at center azimuth, for each aspect, overlaying scaled vehicle image.

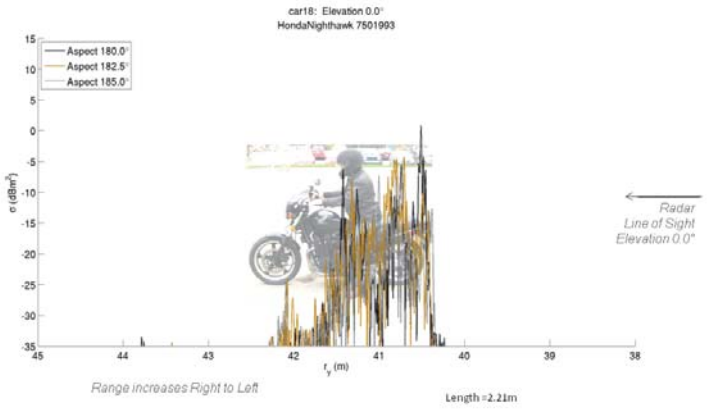

(a) Honda Nighthawk 750 (1993) returns at 0.0° in elevation

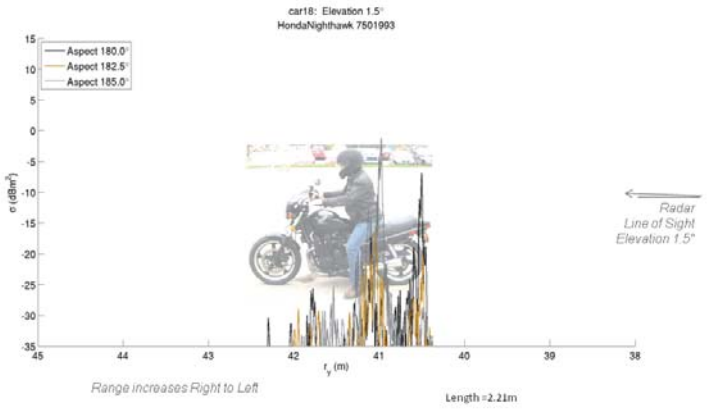

(b) Honda Nighthawk 750 (1993) returns at 1.5° in elevation

Figure 27: Honda Nighthawk 750 (1993) W-band radar returns at center azimuth, for each aspect, overlaying scaled vehicle image.

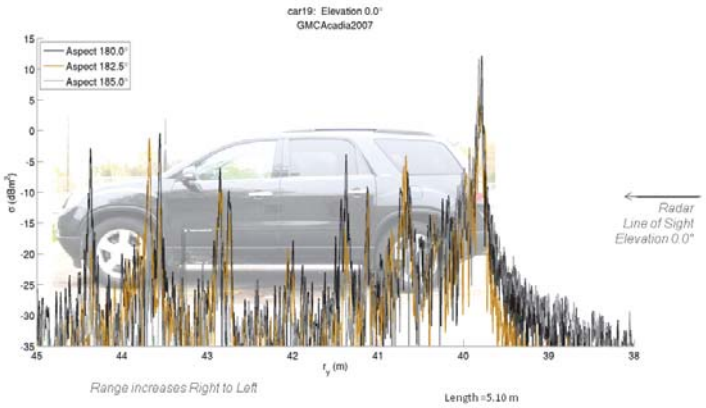

(a) GMC Acadia (2007) returns at 0.0° in elevation

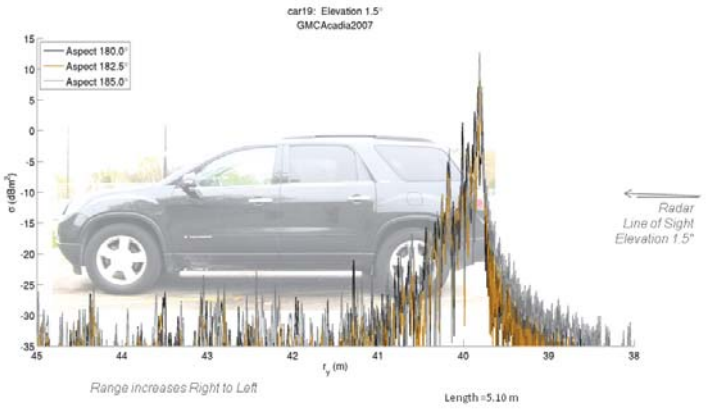

(b) GMC Acadia (2007) returns at 1.5° in elevation

Figure 28: GMC Acadia (2007) W-band radar returns at center azimuth, for each aspect, overlaying scaled vehicle image.

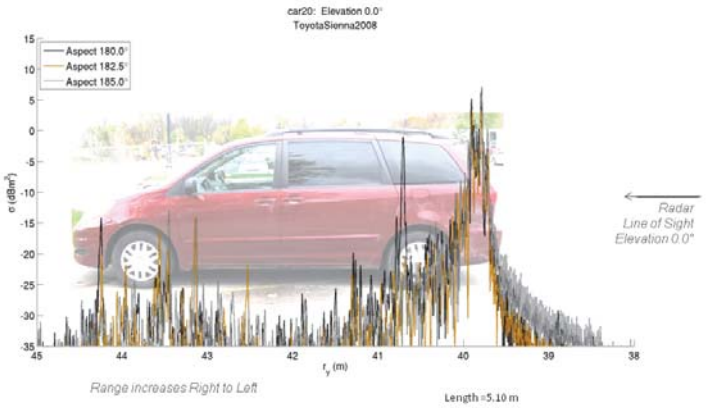

(a) Toyota Sienna (2008) returns at 0.0° in elevation

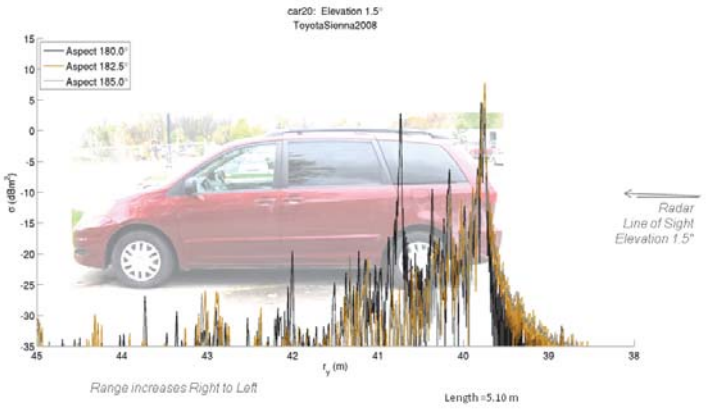

(b) Toyota Sienna (2008) returns at 1.5° in elevation

Figure 29: Toyota Sienna (2008) W-band radar returns at center azimuth, for each aspect, overlaying scaled vehicle image.

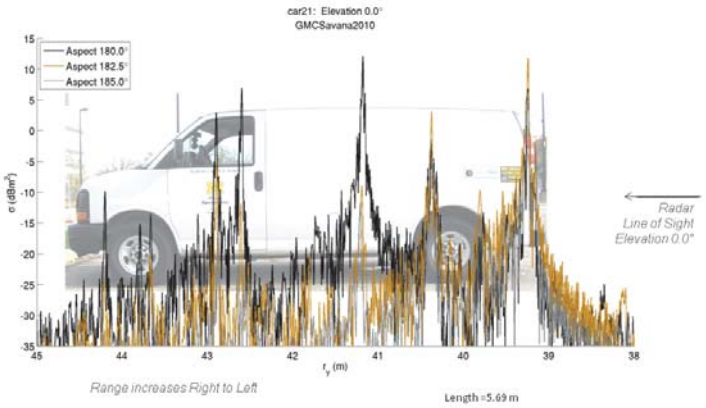

(a) GMC Savana (2010) returns at 0.0° in elevation

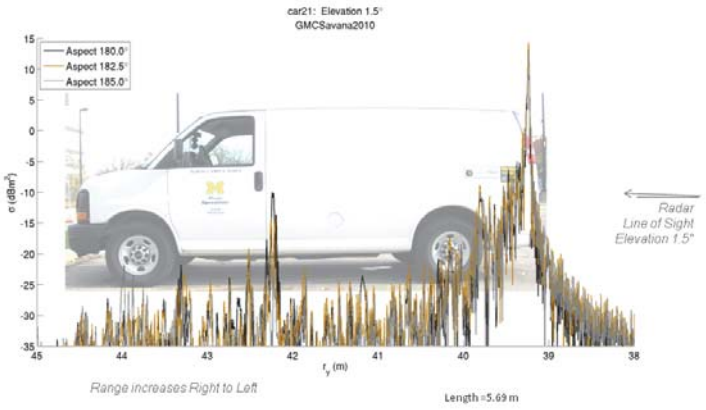

(b) GMC Savana (2010) returns at 1.5° in elevation

Figure 30: GMC Savana (2010) W-band radar returns at center azimuth, for each aspect, overlaying scaled vehicle image.

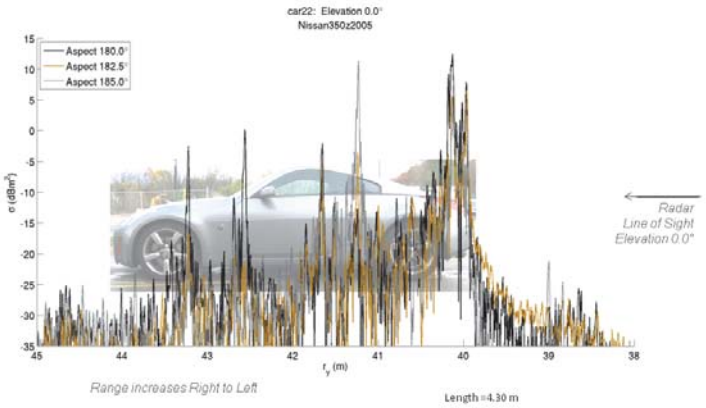

(a) Nissan 350z (2005) returns at 0.0° in elevation

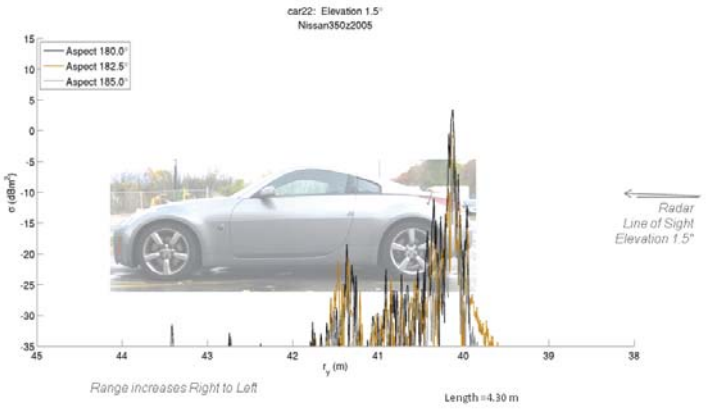

(b) Nissan 350z (2005) returns at 1.5° in elevation

Figure 31: Nissan 350z (2005) W-band radar returns at center azimuth, for each aspect, overlaying scaled vehicle image.

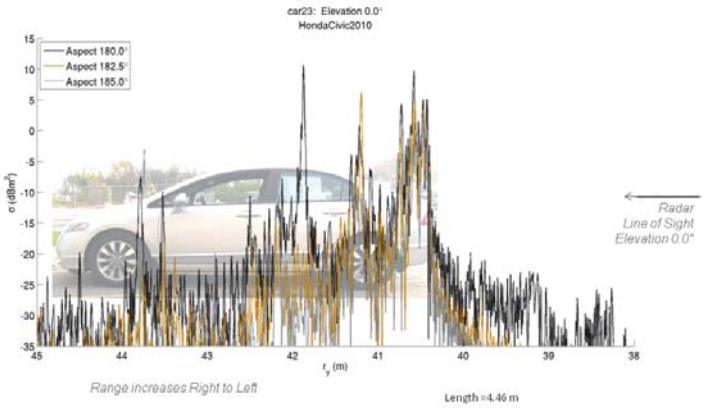

(a) Honda Civic (2010) returns at 0.0° in elevation

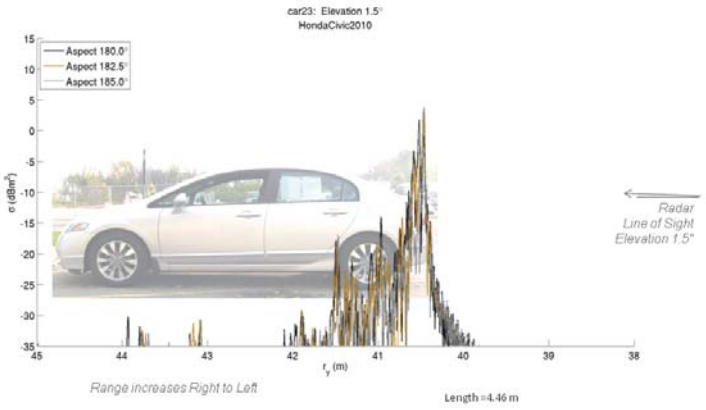

(b) Honda Civic (2010) returns at 1.5° in elevation

Figure 32: Honda Civic W-band radar returns at center azimuth, for each aspect, overlaying scaled vehicle image.

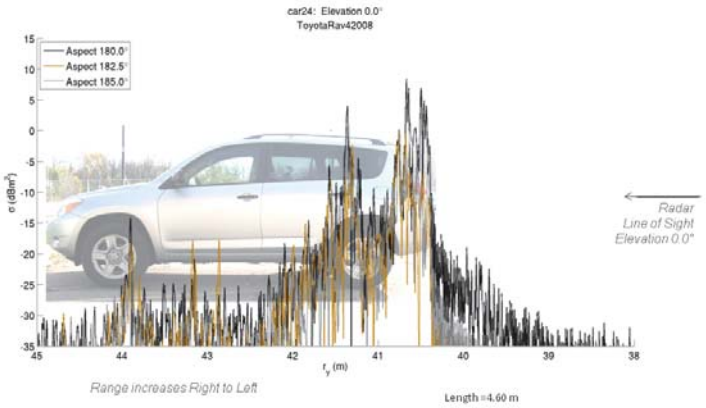

(a) Toyota Rav4 (2008) returns at 0.0° in elevation

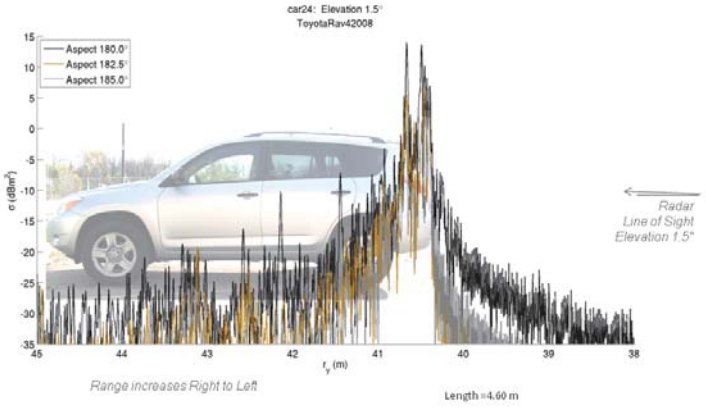

(b) Toyota Rav4 (2008) returns at 1.5° in elevation

Figure 33: Toyota Rav4 (2008) W-band radar returns at center azimuth, for each aspect, overlaying scaled vehicle image.

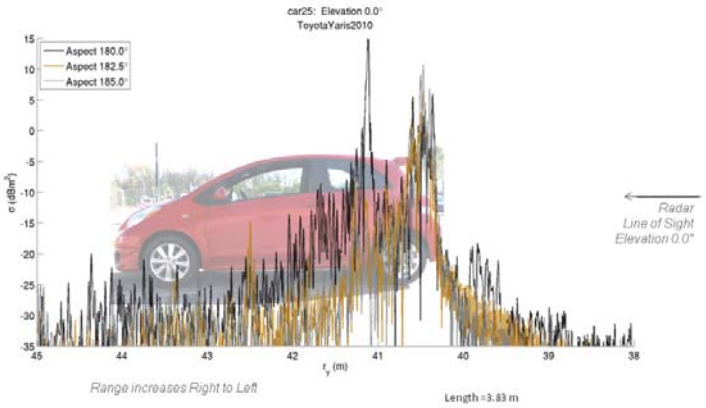

(a) Toyota Yaris (2010) returns at 0.0° in elevation

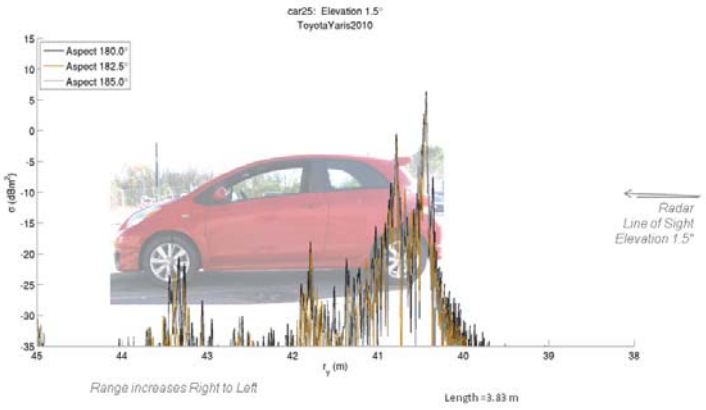

(b) Toyota Yaris (2010) returns at 1.5° in elevation

Figure 34: Toyota Yaris (2010) W-band radar returns at center azimuth, for each aspect, overlaying scaled vehicle image.

5.4 Comparison with Prior Work

In September 1997, the final report Characterization and Evaluation of a Forward-Looking Automotive Radar Sensor for the Discretionary Cooperative Agreement with the National Highway Traffic Safety Administration (NHTSA Grant DTNH22-94-Y-17016), contributed to the knowledge and understanding of radar sensing in roadway environments by conducting structured testing of TRWs prototype forward-looking automotive radar sensor in real-world freeway settings. As part of the effort, the research team measured the radar cross-sections of representative auto-mobiles and roadway objects. The data from this program was stored at www.erim.org/Trans/roadobj/. However, the data is no longer available from this source. The research team for the current effort was able to contact Paul Zoratti, one of the principal researchers for that prior effort, but were unable to locate any of the original data. What does survive are the example plots from the final report. The radar parameters, in Table 4, are sufficiently similar to the current work that we can compare the results, even though limited examples exist.

Table 4: Radar parameters for 1994-1997 study conducted by ERIM

Parameter	W-band Spec
Mode of Operation	Linear-FM Pulsed
Center Frequency	94 GHz
Bandwidth	2 GHz
Transmitted Power	100 mW
Polarization	H-H
Waveform Repetition Freq	2 Hz

In [7], the automotive radar was investigated for the purposes of Intelligent Cruise Control and mitigating rear-end collisions. Therefore, the return levels from vehicles when illuminated from the rear (i.e., a 180 degree aspect angle) were featured prominently From [7], "In evaluating the aspect profiles of the various vehicles measured in this effort, it was observed, as expected, that all of them except the motorcycle provided a significant return at 180 degrees due to specular reflections from the rear structure of the vehicles. It was also observed that as one deviated from the 180 degree view, the return level dropped off at various rates, based on the geometric shape of the vehicle. Table 5 shows the minimum angular departure from a 180 degree aspect

at which the RCS of the vehicle drops below the specified value. For example, the reflectivity of a Taurus was observed to drop below 5 dBm^2 when the aspect angle was below 170 degrees or above 190 degrees. The measured RCS values in [7] are in reasonable agreement with the current study The collections at ERIM were conducted in a grass field and exhibit a higher clutter level than the measurements reported here, which were conducted in an asphalt parking lot.

Table 5: Characteristic Radar Cross-Section fall-off results table reported from 1994-1997 study conducted by ERIM. The parameter θ is the angle of departure from 180° necessary to cause the RCS variation indicated.

Vehicle	θ: RCS $>$ 0 dBm^2	θ: RCS $>$ 5 dBm^2	θ: RCS $>$ 10 dBm^2
Jeep	+180	+180	+5
Taurus	+20	+10	+5
Geo Metro	+40	+30	+5
Corvette	+30	+10	0
Motorcycle	+2	0	0

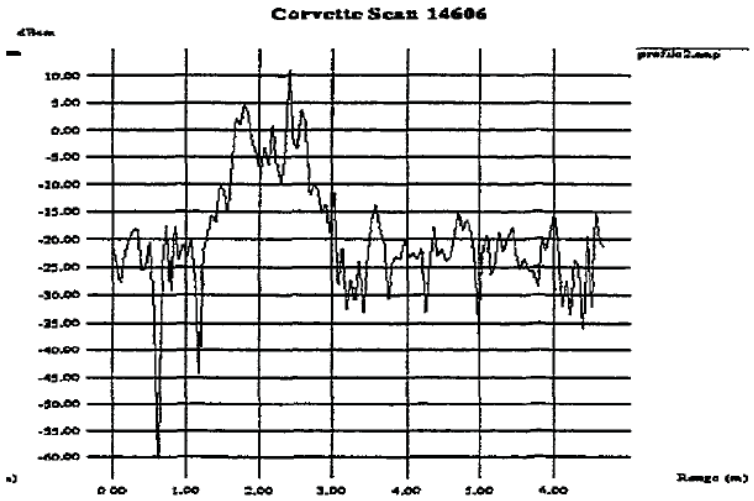

Figure 35: W-band radar scan of a Corvette, viewed at 180°, from ERIM report to NHTSA shows the following resemblance to similar measurements made by MTRI: the majority of scattering occurs within the first meter of the bumper, peak scattering strength is 10 dBm^2, background clutter is -20 dBm^2

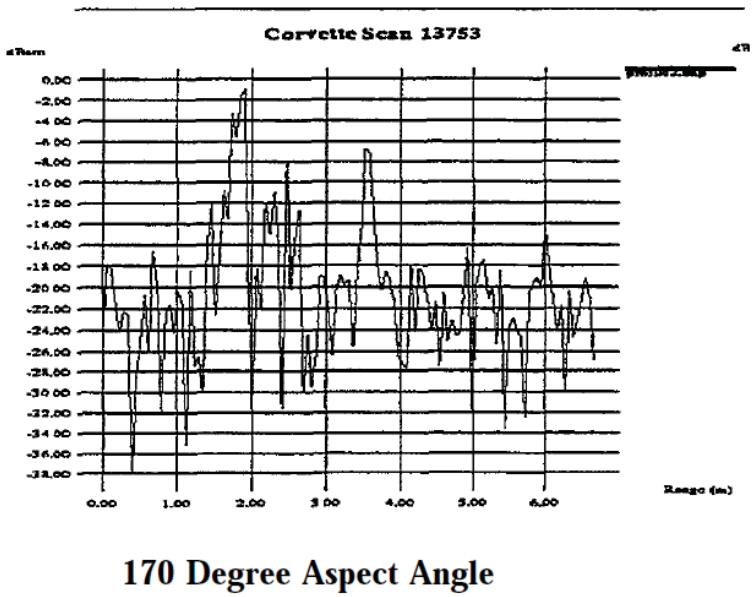

Figure 36: W-band radar scan of a Corvette, viewed at 170°, from ERIM report to NHTSA shows the following resemblance to similar measurements made by MTRI: scattering sources appear further down range along the body, peak scattering strength is reduced by an order of magnitude from tail-on 0 dBm^2, background clutter is -20 dBm^2

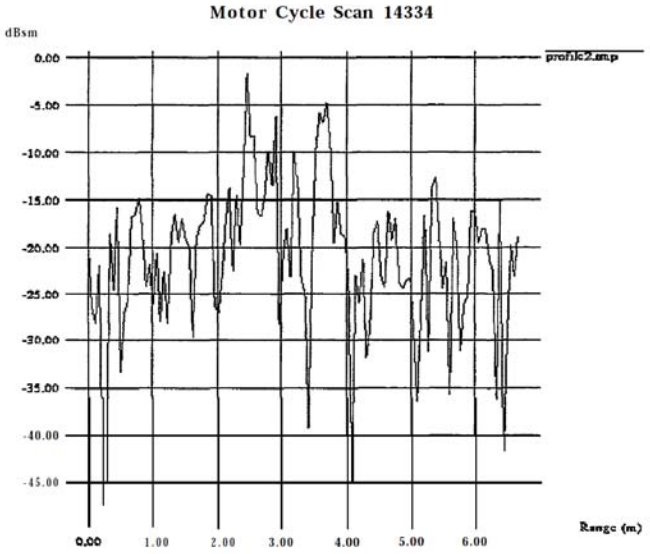

Figure 37: W-band radar scan of a motor cycle, viewed at 180°, from ERIM report to NHTSA shows the following resemblance to similar measurements made by MTRI: the scattering is between 0 and -5 dBm^2 background clutter is -20 dBm^2

5.5 NHTSA SS_V, Test Surrogates

MTRI has measured the SS_V in two configurations. The first configuration is labelled SS_V1 and measurements of the target are addressed in 5.5.1 and 5.5.5. The NHTSA SS_V1 and NHTSA SS_V2 are set on a track that allows the target to recoil following impact in crash tests. Radar reflections from the test surrogate's rail system shows strong reflections only from the leading edge, visible in Figure 38, which is not significant when the surrogate is in place. The subsequent rails down range, with radar absorber in critical locations, are found to be below -20 dB square meters, which is consistent with ground clutter.

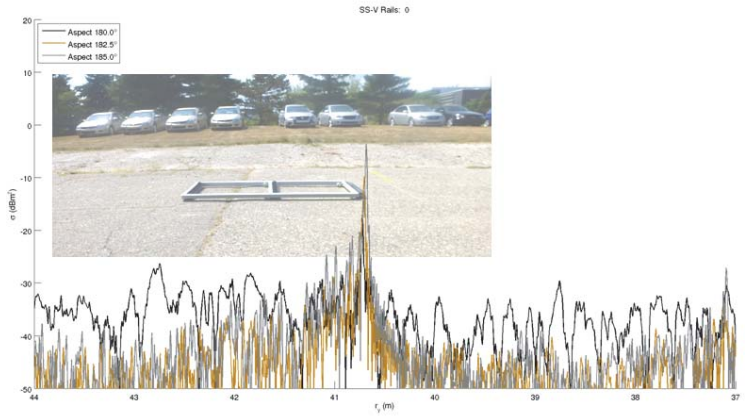

Figure 38: NHTSA SS_V Surrogate Rails Reflectance at

During the analysis of the collections the measurements made against the SS_V1 and the Ford Fiesta were found to be made at higher elevation than the corresponding measurements for the SS_V2. The difference is confirmed with the bore-sight photographs shown in Figure 39. The collections were separated by two months and the site had been dismantled and reassembled. In both test cases (Aug and Oct), the line-of-sight between the radar and the vehicle in the 0.0° elevation case was determined to be level using an inclinometer. The difference in the two collects is that the placement of the translation stage and the vehicle was slightly different, and due to the uneven terrain of the collection site, this resulted in different elevation aimpoints in the two collects. This discrepancy is particularly noticeable in the data collected at the higher elevation. The SS_V1 collection at 1.5° is covering

much less of the target and, in comparison to the data collected on the SS_V2, suffers a loss of more than 10 dB. The radar illumination is a 1 meter diameter circle at this range. At the lower elevation, the center of illumination is near the top of the SS_V1's bumper, whereas, the center of illumination is near the bottom of the SS_V2's bumper.

This analysis explains the dramatic differences observed in measurements of the SS_V1 and SS_V2 at higher elevations and makes clear that future collections should adjust the measurement practices so that beam elevation settings are confirmed with bore-sight photographs.

(a) Boresight scope image for collection at 0.0° elevation of SS_V1

(b) Boresight scope image for collection at 0.0° elevation of SS_V2

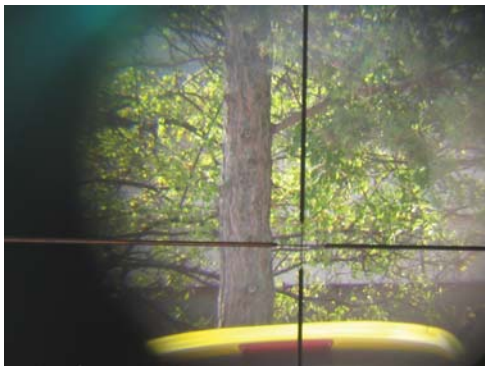

(c) Boresight scope image for collection at 1.5° elevation of SS_V1

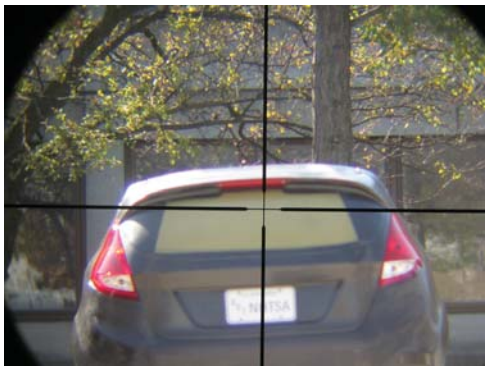

(d) Boresight scope image for collection at 1.5° elevation of SS_V2

Figure 39: Aimpoint elevation difference between August collection of NHTSA SS_V1 and October collection of NHTSA SS_V2.

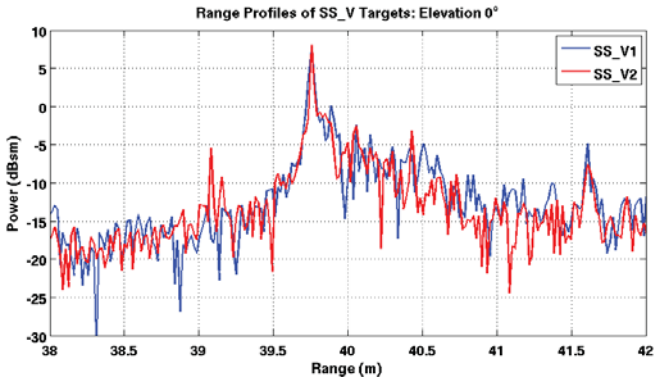

(a) Comparison of NHTSA SS_V1 and SS_V2 at 0.0° in elevation with different bore-sight locations

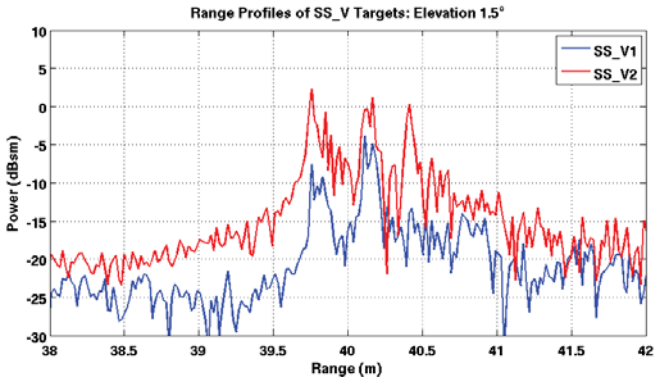

(b) Comparison of NHTSA SS_V1 and SS_V2 at 1.5° in elevation with different bore-sight locations

Figure 40: Range profiles collected on SS_V1 and SS_V2 with different setup. The displacement in elevation produces very small returns from the SS_V1 at the higher elevation setting because the beam is mostly above the target. The elevation setting has less impact on the low elevation data because both targets are largely centered in the illumination region.

5.5.1 NHTSA SS_V1 Reflectance at W-Band

The NHTSA SS_V1 resembles the Ford Fiesta hatchback from the rear-aspect, Figure 41. The surrogate only extends forward to the middle of the rear wheel, as seen in Figure 42. The MTRI W-band radar has a resolution of approximately 2 cm. Overlaying plots of the radar returns on a scaled side-view image of the surrogate allows us to better understand the source of significant radar reflections. Overlay plots are shown for horizontal viewing of the target and when the radar is aimed up in elevation by 1.5°, Figure 43.

Figure 41: NHTSA SS_V1 Test Surrogate - Rear View

5.5.2 NHTSA SS_V1 Reflectance at Ka-Band

The MTRI Ka-band radar also scans 8 GHz of bandwidth and has a resolution of approximately 2 cm. Overlaying plots of the radar returns on a scaled side-view image of the surrogate allows us to better understand the source of significant radar reflections. Radar returns at Ka-band are shown for horizontal viewing of the target and when the radar is aimed up in elevation by

Figure 42: NHTSA SS_V1 Test Surrogate - Side View

0.0° and **1.0**°, Figure 44. The Ka-band collections on August 5, 2012 were made at 1.0° in elevation rather than 1.5° in elevation.

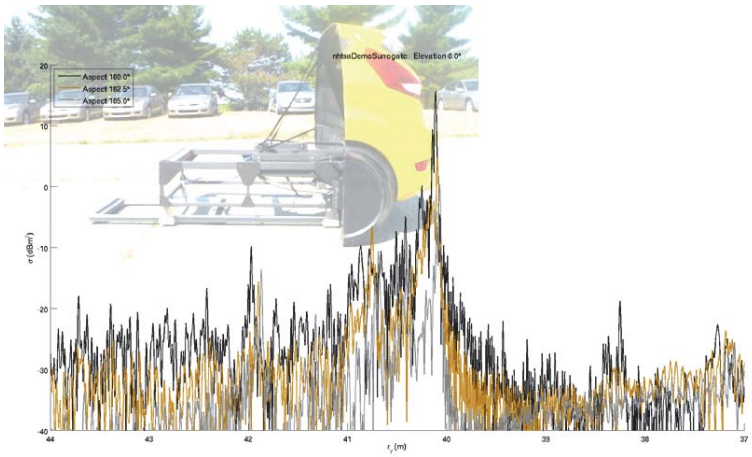

(a) NHTSA SS_V1 Test Surrogate returns at 0.0° in elevation

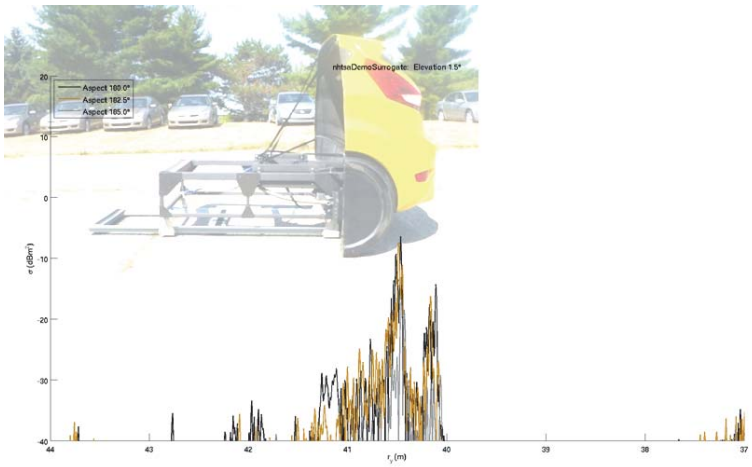

(b) NHTSA SS_V1 Test Surrogate returns at 1.5° in elevation

Figure 43: W-band range profiles of NHTSA SS_V1 Test Surrogate, collected on August 5, 2012, overlaid on photograph scaled to plot. The range profiles are collected at elevation of 0.0° and 1.5° and azimuths of 180.0° (black), 182.5° (gold) and 185.0° (silver). Relative to the measurements made against the SS_V2, the elevation is biased up by 0.4° higher.

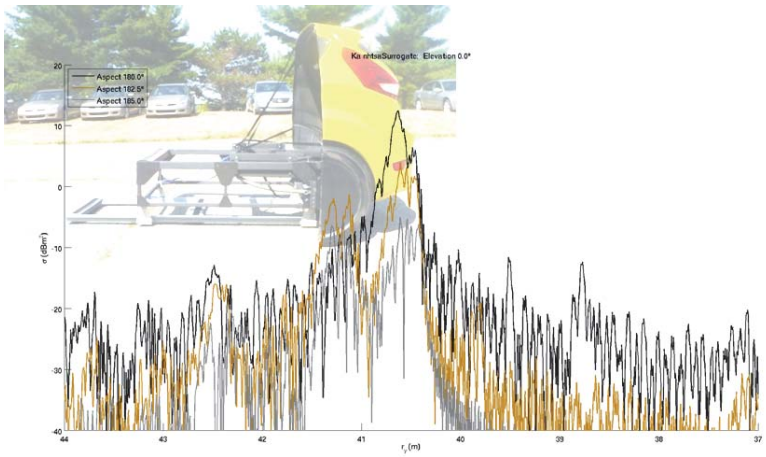

(a) NHTSA SS_V1 Test Surrogate returns at 0.0° in elevation

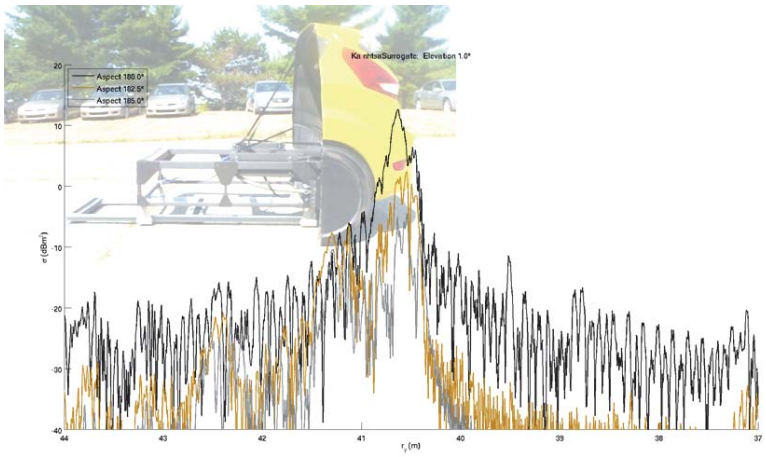

(b) NHTSA SS_V1 Test Surrogate returns at 1.0° in elevation

Figure 44: Ka-band range profiles of NHTSA SS_V1 Test Surrogate, collected on August 5, 2012, overlaid on photograph scaled to plot. The range profiles are collected at an elevation of 0.0° and 1.0° and azimuths of 180.0° (black), 182.5° (gold) and 185.0° (silver). Relative to the measurements made against the SS_V2, the elevation is biased up by 0.4° higher.

5.5.3 NHTSA SS_V2 Reflectance at W-Band

The NHTSA SS_V2 Test Surrogate resembles the Ford Fiesta hatchback from the rear-aspect, Figure 45. The surrogate only extends forward to the middle of the rear wheel, as seen in Figure 46. Note that unlike those used for SS_V1, all figures showing SS_V2 in this report present the surrogate without the vinyl wrap used to simulate painted surfaces and tinted rear glass, as this was added after the radar return measurements discussed subsequently were performed. The MTRI W-band radar has a resolution of approximately 2 cm. Overlaying plots of the radar returns on a scaled side-view image of the surrogate allows us to better understand the source of significant radar reflections. Overlay plots are shown for horizontal viewing of the target and when the radar is aimed up in elevation by 1.5°, Figure 47. The NHTSA SS_V2 has been modified to produce a more realistic set of returns by rounding the top leading edge of the rear bumper, adding a radar absorbing mat to the inside of its rear bulkhead, and replacing a section of the surrogates carbon fiber shell with a Kevlar panel to reduce the mirror like quality of the SS_V1, especially at Ka-band. [1]

5.5.4 NHTSA SS_V2 Reflectance at Ka-Band

The MTRI Ka-band radar also scans 8 GHz of bandwidth and has a resolution of approximately 2 cm. Overlaying plots of the radar returns on a scaled side-view image of the surrogate allows us to better understand the source of significant radar reflections. Radar returns at Ka-band are shown for horizontal viewing of the target and when the radar is aimed up in elevation by 0.0° and 1.5°, Figure 48.

[1] Kevlar is a trademarked name for a synthetic fiber product developed by E. I. du Pont de Nemours and Company.

Figure 45: NHTSA SS_V2 Test Surrogate - Rear View.

Figure 46: NHTSA SS_V2 Test Surrogate - Side View. In the foreground is an orange pylon supporting radar absorbing tile to reduce high clutter response from a manhole cover with an elevated rim.

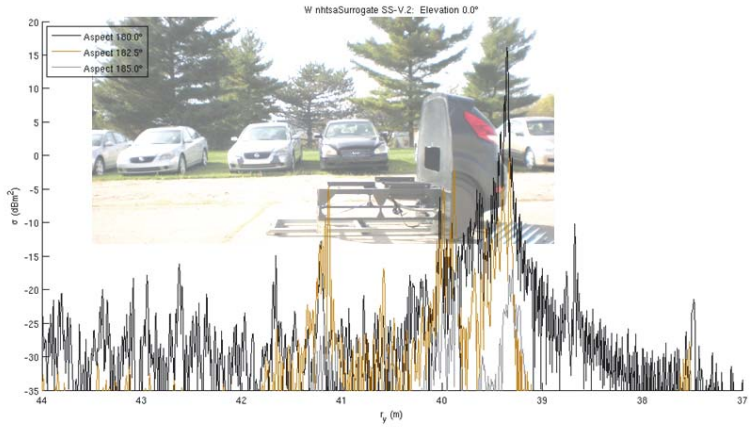

(a) NHTSA SS_V2 Test Surrogate returns at 0.0° in elevation

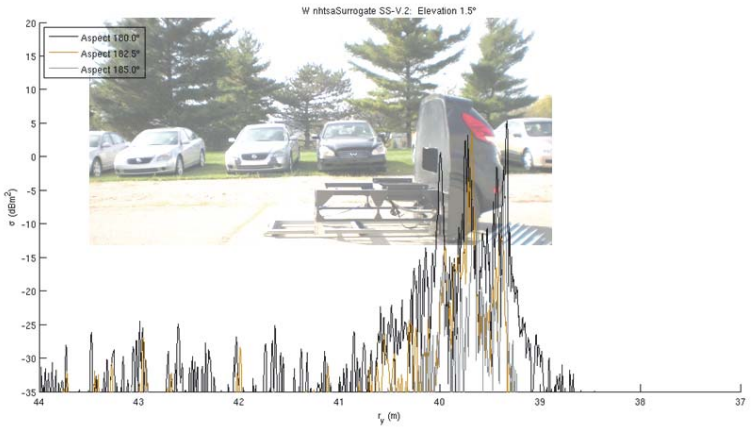

(b) NHTSA SS_V2 Test Surrogate returns at 1.5° in elevation

Figure 47: W-band range profiles of NHTSA SS_V2 Test Surrogate, collected on October 11, 2012, overlaid on photograph scaled to plot. The range profiles are collected at elevation of 0.0° and 1.5° and azimuths of 180.0° (black), 182.5° (gold) and 185.0° (silver).

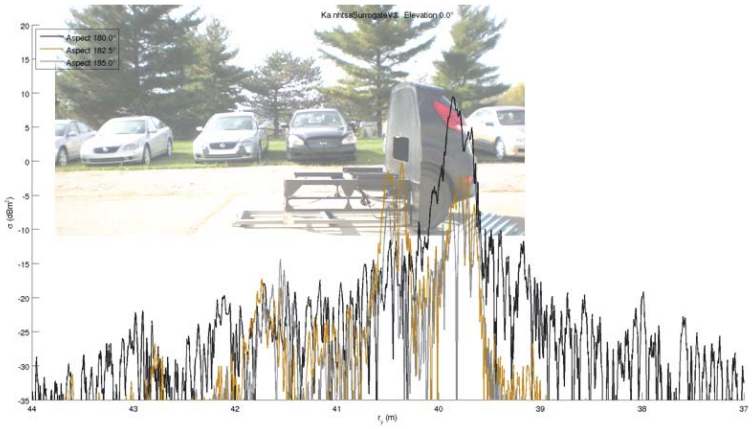

(a) NHTSA SS_V2 Test Surrogate returns at 0.0° in elevation

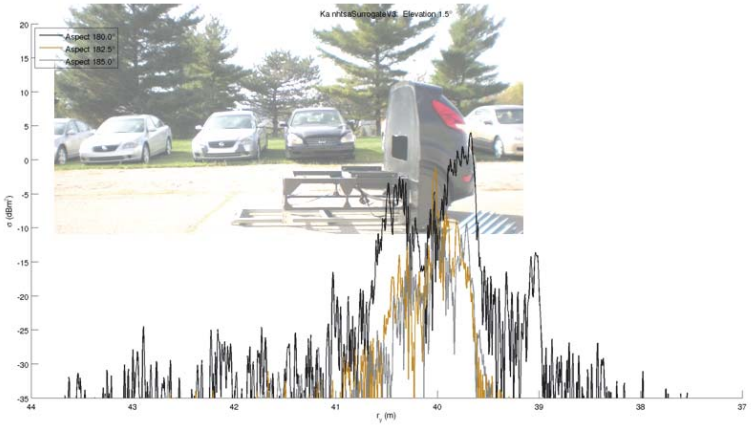

(b) NHTSA SS_V2 Test Surrogate returns at 1.5° in elevation

Figure 48: Ka-band range profiles of NHTSA SS_V2 Test Surrogate, collected on October 11, 2012, overlaid on photograph scaled to plot. The range profiles are collected at an elevation of 0.0° and 1.5° and azimuths of 180.0° (black), 182.5° (gold) and 185.0° (silver).

5.5.5 NHTSA SS_V2 Design Improvements

The NHTSA SS_V design incorporates a flat-plate strike zone that mechanically allows the surrogate to recoil along its rails. It was noted in SS_V1 as a source of scattering that is not typical for most auto-mobiles. The principal concern is that the radar response of the target changes more dramatically moving from 180° to a few degrees in either direction. If used in tests where the striking vehicle is approaching from 180°, then this is not a concern. To extend the utility of the SS_V as a test surrogate at greater approach angles, the team of engineers from MTRI and NHTSA designed and experimented with ideas to improve the SS_V's signature for scenarios with angles further from tail-on. One idea is to place a cylindrical element on the target so that scattering would not fall off as quickly. Theoretically, a thin band (7 centimeters), bent into a cylinder with a 1 meter radius of curvature would provide an element with a notional 5 dBm^2 source over a broad range of aspects. A configuration that showed promise in the field is shown in Figure 49.

(a) W-band errors. (b) Ka-band errors.

Figure 49: NHTSA SS_V2 Test Surrogate with metal band attached to rear bumper. This is an improvised design intended to provide greater angular support.

The modification of the SS_V2 in the field by attaching a metal band mounted directly on the rear-bumper as shown in Figure 49, indeed, shows a greater response at angles away from 180.0°. Only the three range profiles

shown in Figure 50 were collected, so we do not have sufficient data to compare the Weibull parameters, but intuition is that this greater support can only increase the shape factor.

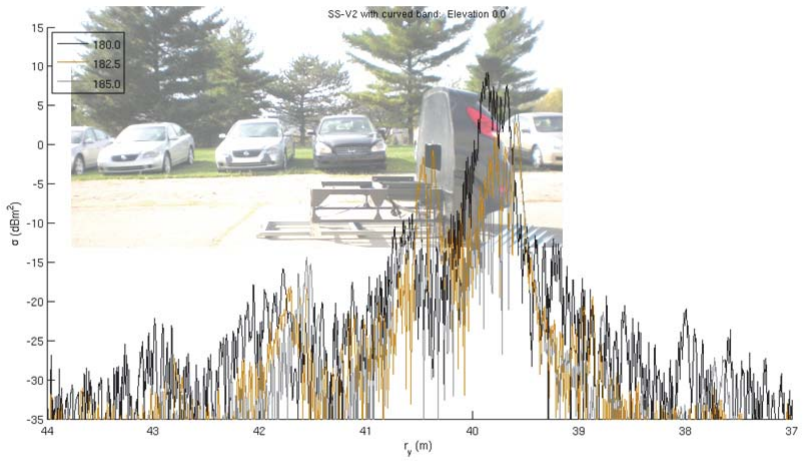

Figure 50: Range profiles of NHTSA SS_V2 Test Surrogate with metal band demonstrates improved angular support.

An attempt to modify the SS_V2 in the field shows a metal band mounted beneath the rear-bumper as shown in Figure 51; however, did not produce the desired angular support. The measurements are shown in Figure 52. One can conjecture that the mounting did not provide the desired reflections because the metal strip is flat and may have been tipped in elevation relative to the radar. Other shape elements can be considered to provide the correct scattering support.

Figure 51: NHTSA SS_V2 Test Surrogate with metal band mounted under bumper.

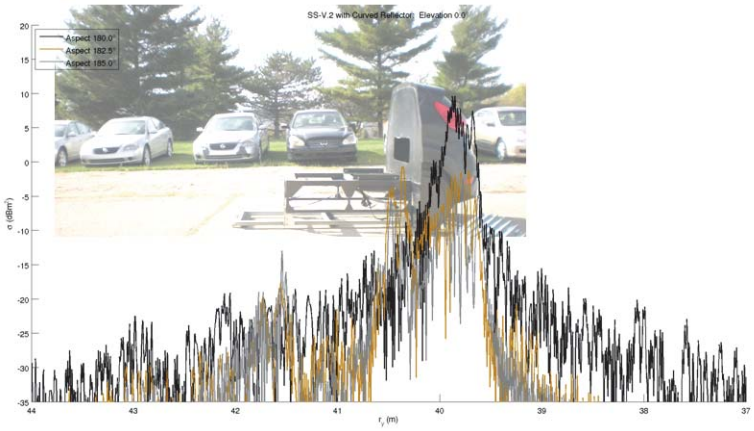

Figure 52: Ka-band range profiles of NHTSA SS_V2 Test Surrogate with a curved metal band attached to the bottom of the bumper, collected on October 11, 2012, overlaid on photograph scaled to plot. The range profiles are collected at an elevation of 1.5° and azimuths of 180.0° (black), 182.5° (gold) and 185.0° (silver).

5.6 Other Test Surrogates

MTRI has measured a Helly-Hensen balloon car and two of NHTSA's foam car test surrogates. A major concern with each of these targets, from a radar perspective, is that the targets rapidly fluctuate independently from changes in aspect. Such behavior is likely to be found in traffic when vehicles have soft material coverings, such as a tarp covered truck-bed, softly covered furniture and towed recreational vehicles under loose covers. However, this is a minority of vehicles. Most vehicles will fluctuate more slowly if the geometry is slowly changing than these surrogate targets.

5.6.1 NHTSA FC-1, Reflectance at W-Band

The NHTSA Foam Car 1, FC-1 Test Surrogate is shown from the rear-aspect, Figure 53. The surrogate only extends forward to the middle of the rear wheel, as seen in Figure 54. The MTRI W-band radar has a resolution of approximately 2 cm. Overlaying plots of the radar returns on a scaled side-view image of the surrogate allows us to better understand the source of significant radar reflections. Overlay plots are shown for horizontal viewing of the target and when the radar is aimed up in elevation by 1.5°, Figure 55.

Figure 53: NHTSA Foam Car FC-1 Test Surrogate - Rear View

Figure 54: NHTSA Foam Car FC-1 Test Surrogate - Side View

5.6.2 Helly-Hensen Balloon Car, Reflectance at W-Band

The Helly-Hensen Balloon Car Test Surrogate is shown from the rear-aspect, Figure 56. The surrogate extends a little over 3 meters, as seen in Figure 57. The MTRI W-band radar has a resolution of approximately 2 cm. Overlaying plots of the radar returns on a scaled side-view image of the surrogate allows us to better understand the source of significant radar reflections. Overlay plots are shown for horizontal viewing of the target and when the radar is aimed up in elevation by 1.5°, Figure 58. The balloon car has a very physical low-profile and its radar reflectance is very small if the angle of view is elevated. The balloon car is semi-transparent at W-band so that we see reflections from the front of the vehicle, as well as, the rear. Aside from the rapid fluctuation of the soft-cover targets, the Helly-Hensen Balloon Car produces a signature from the rear and front, separated by approximately 3 meters with no significant reflections between. This behavior is not observed in the vehicles.

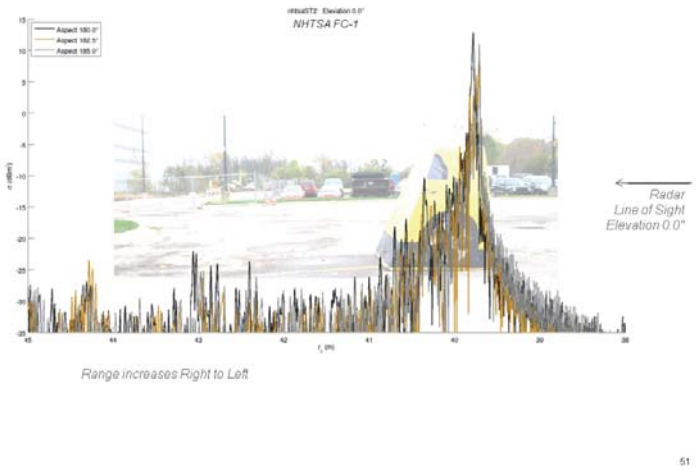

(a) NHTSA Foam Car FC-1 returns at 0.0° in elevation

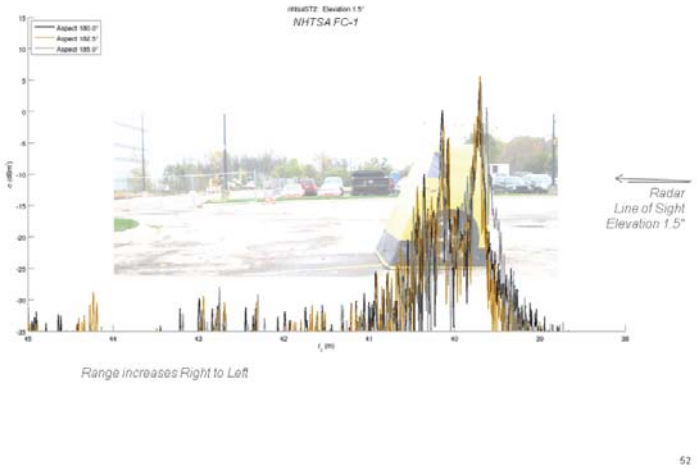

(b) NHTSA Foam Car FC-1 returns at 1.5° in elevation

Figure 55: W-band range profiles of NHTSA Foam Car FC-1, collected on October 26, 2011, overlaid on photograph scaled to plot. The range profiles are collected at elevation of 0.0° and 1.5° and azimuths of 180.0° (black), 182.5° (gold) and 185.0° (silver).

Figure 56: Helly-Hensen Balloon Test Surrogate - Rear View

Figure 57: Helly-Hensen Balloon Test Surrogate - Side View

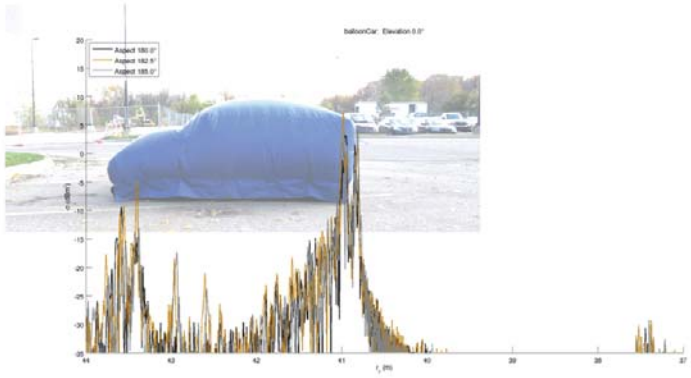

(a) Helly-Hensen Balloon Car returns at 0.0° in elevation

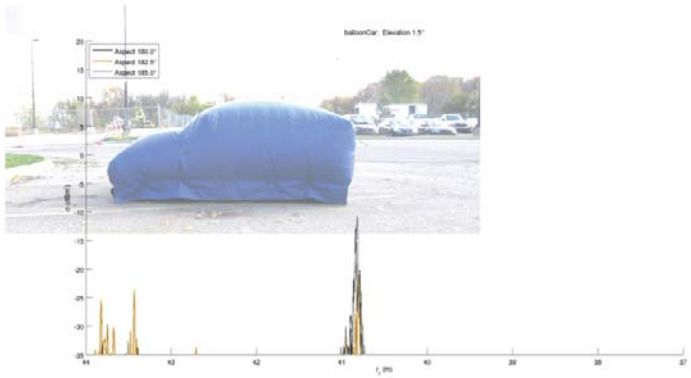

(b) Helly-Hensen Balloon Car returns at 1.5° in elevation

Figure 58: W-band range profiles of Helly-Hensen Balloon Car, collected on October 28, 2011, overlaid on photograph scaled to plot. The range profiles are collected at elevation of 0.0° and 1.5° and azimuths of 180.0° (black), 182.5° (gold) and 185.0° (silver).

5.6.3 NHTSA FC-2, Reflectance at W-Band

The NHTSA FC-2 Test Surrogate, Figure 59, resembles the FC-1 from the rear-aspect. The surrogate only extends forward to the middle of the rear wheel, as seen in Figure 60. The MTRI W-band radar has a resolution of approximately 2 cm. Overlaying plots of the radar returns on a scaled side-view image of the surrogate allows us to better understand the source of significant radar reflections. Overlay plots are shown for horizontal viewing of the target and when the radar is aimed up in elevation by 1.5°, Figure 61.

Figure 59: NHTSA Foam Car FC-2 Test Surrogate - Rear View

Figure 60: NHTSA Foam Car FC-2 Test Surrogate - Side View

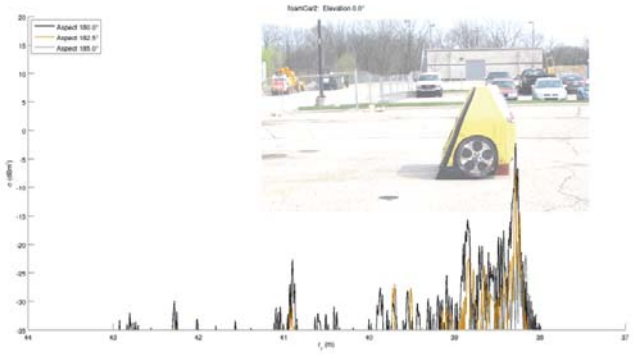

(a) NHTSA Foam Car FC-2 returns at 0.0° in elevation

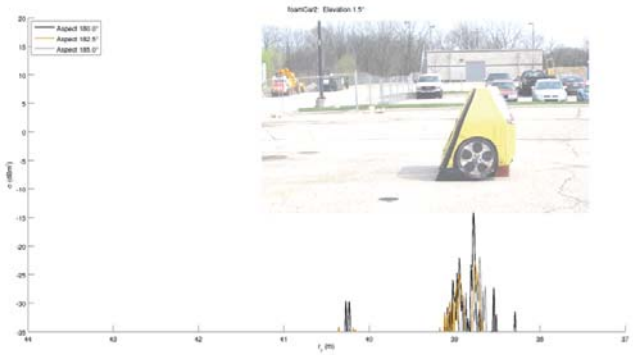

(b) NHTSA Foam Car FC-2 returns at 1.5° in elevation

Figure 61: W-band range profiles of NHTSA Foam Car FC-2, collected on March 28, 2012, overlaid on photograph scaled to plot. The range profiles are collected at elevation of 0.0° and 1.5° and azimuths of 180.0° (black), 182.5° (gold) and 185.0° (silver).

6 Method of Analysis

6.1 Evaluation Approach

The performance of radar detection and tracking systems are characterized by the radar parameters, the scattering of targets and the environment. It has long been recognized that statistical models allow radar engineers to predict the performance of radar systems [8]. By the same reasoning, we can measure the performance of radar systems using *surrogate* targets that have the same statistical model as the *real* targets. The statistical models developed from the measurements are used to estimate the detector error trade-offs [9] in Section 8.3

The varied angle and frequency measurements discussed in Section 4.1 are used to generate a probability density function of the measured radar cross-sections. The same measurement procedure is used to evaluate surrogate test targets. The wideband response of the vehicles, viewed at multiple rear-aspects, is analyzed statistically. A wideband radar-cross section (RCS), to provide a robust metric [4], is used to characterize the scattering.

The measurements here are not typical RCS target models, as the statistic is developed from sparse sampling in angle and over a wideband. However, they do serve two purposes: 1.) to understand RF reflections from many vehicles and 2.) to develop an RCS statistic that may be used to evaluate surrogate targets.

The fluctuation model developed for the targets in our test is valid for the sampling with this collection geometry. The fluctuation model for a vehicle at rear aspect during a crash scenario, would be populated by a dense sampling of radar reflections from a smaller angular extent and a larger domain of range. We evaluate the surrogates over the entire collection span, as well as from tail-on only.

6.2 Figures of Merit

Three figures of merit are identified that have direct impact on detection and tracking performance for any radar system. The first is the stability of the target. We first define the terms radar pulse and sweep. In a pulsed-waveform radar, the radar emits a short-burst of energy followed by a relatively long receiving interval. The total time from one pulse start until the next pulse start is termed the pulse-interval. If the radar is further gimbaled to measure

multiple viewing angles, then we refer to the time from a pulse emitted at one viewing angle, until that same viewing angle is repeated, is called the sweep or re-visit interval. In this research, the target and radar are static. The radar is moved to view the target from different aspects, but each measurement is made with a stationary transmitter, receiver and scene. Each measurement is made at least 5 times at approximately 3 Hertz. The variation in those 5 measurements is due to the instability of the target over a 1.5 second collection interval and is not due to variation in the targets angular RCS dependence. The first of our three metrics is the instability of the target as defined by equation 9. If the target instability, ϵ, is large, then it means that the target signature fluctuates significantly independent of the radar's viewing aspect. The automobiles in our test set show low values of target instability. If the surrogate shows a high instability measurement, then it cannot be expected to accurately predict the detection and tracking performance of the radar under test.

$$\epsilon = \langle \frac{\Delta\sigma(f)}{\sigma(f)} \rangle_f \tag{9}$$

The second of our three metrics is the expected value of the radar cross section observed over the span of angles and frequencies measured, as expressed in equation 10. Assuming that the surrogate has a sufficiently low instability, the expected RCS of the target provides a sense of how large the target's reflected power will appear to the radar.

$$\overline{\sigma} = \langle \sigma(f, \theta) \rangle_{f,\theta} \tag{10}$$

While this figure of merit fails to capture the complete statistical fluctuation model, it is relevant because we are still working with a limited sample of vehicles to characterize our statistical model. The third of our three metrics captures the complete statistical fluctuation model represented by our collected angles and frequencies. This is the wideband, angular fluctuation model, based on the best-fit parameters to the Weibull distribution for the radar cross section observed over the span of angles and frequencies measured, as expressed in equation 11

$$P_W(\sigma(\theta, f); \alpha, \beta) = \alpha\beta^{-\alpha}\sigma^{\alpha-1}e^{-(\frac{\sigma}{\beta})^{\alpha}} \tag{11}$$

This is the most demanding of the metrics; and thus, the most dependent on the significance of the sampling. To mitigate this dependence, the same

frequencies and viewing aspects are used to measure the vehicles and the surrogates.

6.3 Selection of statistical model

With the well-known Swerling models for extended target [8] as a starting point, we examined the gamma distribution, Weibull distribution, and log-normal distribution as models for the target-in-clutter data we collected. Our observations show that the best model for our measured data is the Weibull distribution. We first present the measured data, followed by the discussion on the statistical distribution models.

6.3.1 Measured RCS of selected vehicles

Measured radar data is spatially edited to reduce the role of clutter in our model. Each vehicle's data is edited so that the data to be analysed begins 10 cm before the bumper and continues up to some maximum length we will call an acceptance window. The data has been analysed for an acceptance window of both 1.5 meters and 4.0 meters. Radar data from two of the twenty-five vehicles measured are chosen for exhibition. The Toyota Corolla data is included because its Weibull distribution shape and scale parameters reside toward the middle of the twenty-five measured vehicles; a range-profile of the Corolla is shown in Fig. 62, with a 1.5 meter acceptance window highlighted in red. The GMC Sierra, which has its range-profile shown in Fig. 63, is included for two primary reasons. One is that pickup trucks top the list of vehicles most frequently struck in rear-end crashes, as reported by a National Highway transportation Safety Administration study [2]. Secondly, the statistical model demonstrates that the 'shape' of a vehicle, rather than 'size', is the stronger factor in its radar return signal strength. Notice that Fig. 63 shows an acceptance window of 4.0 meters.

The spectral data collected from the Toyota Corolla is shown in Fig. 64, which shows the measured radar cross section (RCS) for a variety of aspect angles, collected over the 91-97 GHz frequency band. This data is discretely sorted into equal-sized linear bins to produce a histogram of the RCS data, and is shown in Figure 65, with the probability density function (PDF) of the best-fitting Weibull distribution plotted in red. The best-fitting PDF is determined from the maximum likelihood estimate (MLE) of the Weibull distribution parameters.

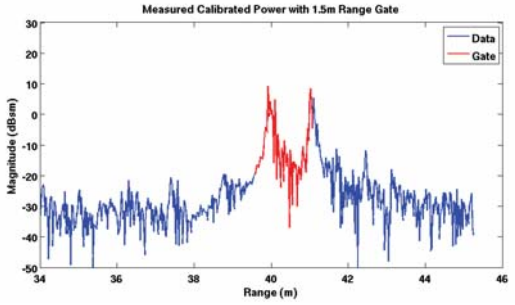

Figure 62: Range profile of Toyota Corolla with software range gate to limit the signature to 1.5 meters, starting from the vicinity of the vehicle's bumper.

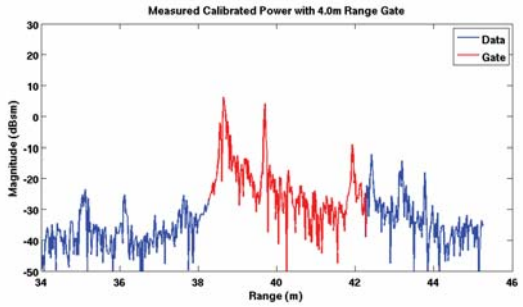

Figure 63: Range profile of GMC Sierra with software range gate to limit the signature to 4.0 meters, starting from the vicinity of the vehicle's bumper.

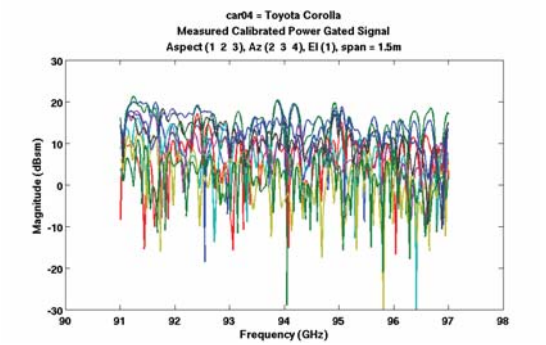

Figure 64: Calibrated spectral response of Toyota Corolla over the band of 91 to 97 GHz. The target data has been spatially edited with a 1.5 meter acceptance window. The plot shows lines representing measurements from several aspect angles.

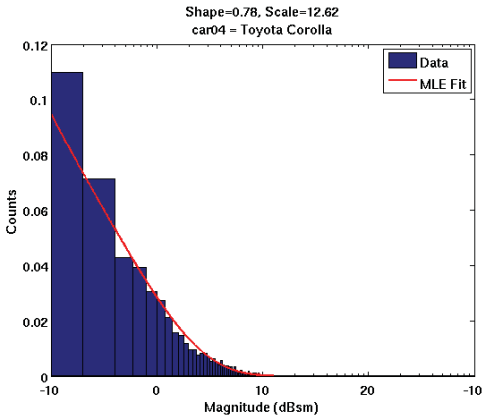

Figure 65: The spectral response of the Toyota Corolla for varied aspects and over the band of 91 to 97 GHz is sorted into bins to produce the histogram here. This histogram is treated as the probability density function for measurements of RCS and is shown along with Weibull distribution described by the maximum likelihood estimated parameters determined from the data.

6.3.2 Goodness of fit

Starting with the Swerling model, a gamma distribution of an extended target, our analysis suggests that the Weibull distribution gives us the best fit for the measured signals; see Figure 66 and Figure 67. These two figures show the Kolmogorov-Smirnov test statistic, a goodness-of-fit metric, for the various distributions we studied: Weibull, Gamma, and log-normal. The normal distribution is included for comparison as well. Fig. 66 is the comparison chart for RCS measurements at 0° elevation - the radar placed directly facing the vehicles' bumper, with a software range-gate of 4.0 meters applied to the data. Figure 67 is the comparison chart for RCS measurements at 1.5° elevation, with a software range-gate of 1.5 meters applied to the data. We note here that the Weibull shows the best fit at 0° elevation radar measurement. However, as radar collection angle is varied from 0° elevation, the Weibull distribution fit becomes less robust in comparison to other distribution fitting. The Weibull distribution arguably gives the best fit for most of the vehicles measured in this data collection campaign.

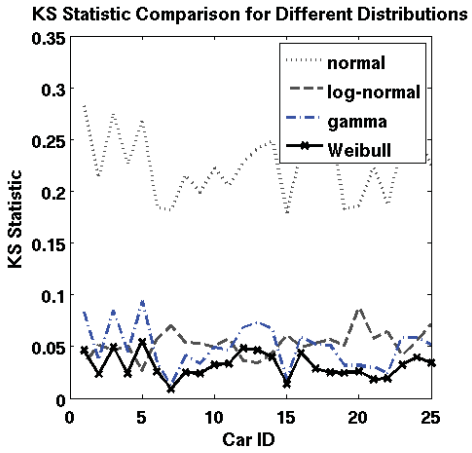

Figure 66: Goodness of fit of the modelled distribution: for 0° elevation and software range-gate of 4 meters

Figure 68 and 69 show the Weibull distribution parameters of measured RCS, with measured data range gated to 1.5 meters and 4 meters, respectively, from the tail of the vehicle and at a measurement tilt angle of 0°. Comparing these two figures, we observed little dependency of the distribu-

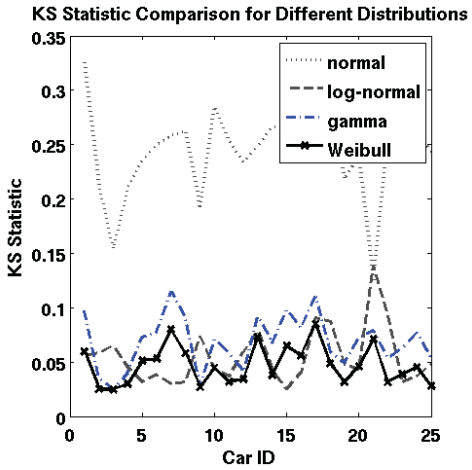

Figure 67: Goodness of fit of the modelled distribution: for 1.5° elevation and software range-gate of 1.5 meters

tion parameters on the range gating applied, presumably because the principal scattering sources are found near (within 1.5 meters of) the bumper. Figure 70 and 71 show the Weibull parameters at measurement tilt angle of 1.5°, at the same range gating of 1.5 meters and 4 meters. Comparing Figure 68 against 70, we noted the effect of raising the antennas view of nearly a meter from bumper height - overall RCS is reduced by approximately 5 dB. Similar observation applies when comparing Figure 69 against 71.

6.3.3 Relevance of statistical result

The measurements here are not traditional target RCS measurements. The measurements are intended to better understand vehicle radar reflections which are likely to be observed by PCS radars. PCS radars operate in clutter and are not guaranteed to be far-field. In fact, because the targets are so large, the far-field assumption may be pathological. PCS radars do not necessarily illuminate the entire target when closing in on a lead vehicle. All of these factors make the work here relevant to the traditional task of estimating target RCS values to allow radar system designers to estimate system performance; yet, the measurements are non-traditional because of the nature of the environment that the systems must perform.

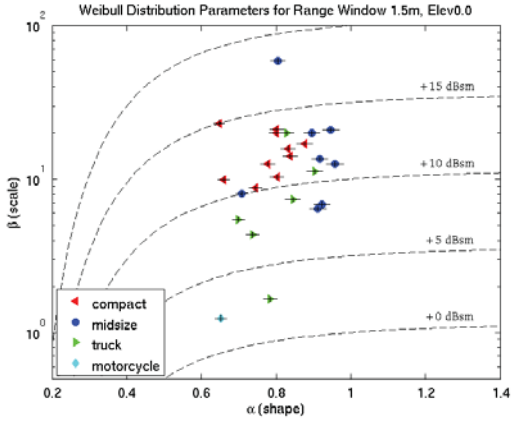

Figure 68: Weibull distribution parameters, $_K$ (shape) and $_X$ (scale), for 25 vehicles viewed at near tail aspects with 1-m diameter radar beam at W-band. Range gating set to 1.5 meters; elevation of 0°. The results of MLE Weibull fit are plotted as icons with bars showing the 95% confidence interval.

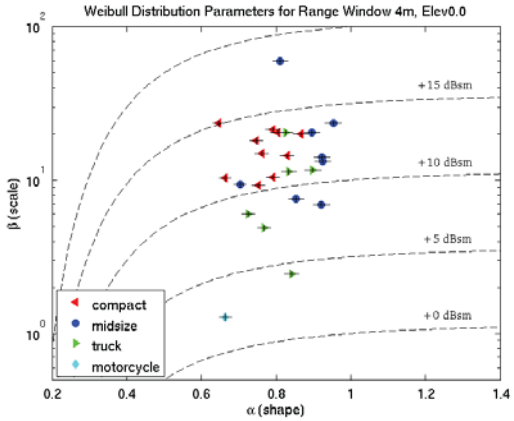

Figure 69: Weibull distribution parameters, $_K$ (shape) and $_X$ (scale), for 25 vehicles viewed at near tail aspects with 1-m diameter radar beam at W-band. Range gating set to 4 meters; elevation of 0°. The results of MLE Weibull fit are plotted as icons with bars showing the 95% confidence interval.

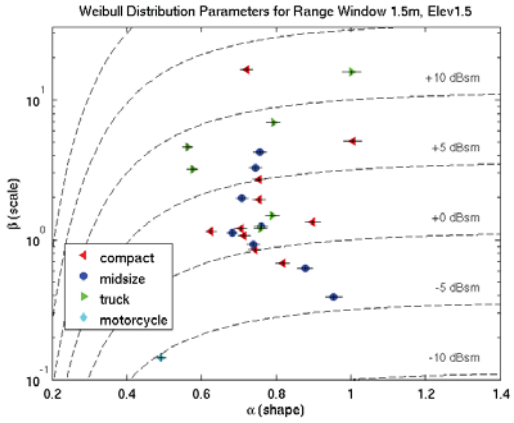

Figure 70: Weibull distribution parameters, $_K$ (shape) and $_X$ (scale), for 25 vehicles viewed at near tail aspects with 1-m diameter radar beam at W-band. Range gating set to 1.5 meters. The results of MLE Weibull fit are plotted as icons with bars showing the 95% confidence interval.

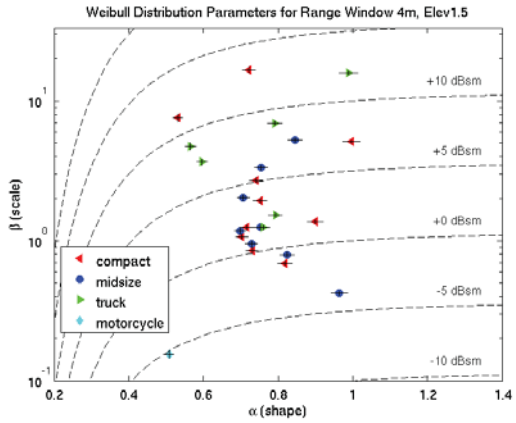

Figure 71: Weibull distribution parameters, $_K$ (shape) and $_X$ (scale), for 25 vehicles viewed at near tail aspects with 1-m diameter radar beam at W-band. Range gating set to 4 meters. The results of MLE Weibull fit are plotted as icons with bars showing the 95% confidence interval.

7 Results

7.1 Evaluation of test surrogates over 5° viewing aspects

We measured twenty-six personal vehicles at W-band from 30 unique viewing angles near rear-aspect, across 8 GHz of bandwidth, to understand the reflections from a lead vehicle observed by a PCS instrumented vehicle. The measurements were repeated for six of the cars at Ka-band. The ensemble of measurements in angle and frequency for each vehicle is treated as a distribution of RCS. The distribution is then fitted by maximum likelihood estimation to several 2-parameter distributions, treating the low and high elevation separately. The Weibull distribution is found to be the best overall fit for the measured data. The Vehicle Domain is estimated from the distributions, which are plotted in Figure 76 and 77, and in general does not consider the Motorcycle as a member. The span of these values, computed for the low elevation (horizontal viewing) is reported for the Vehicle Domain for W-band in Table 6 and at Ka-band in Table 7. These tables allow the reader to determine whether each surrogate is within the Vehicle Domain. None of the surrogates is completely within the Vehicle Domain over the 5° collection window.

Table 6: W-band evaluation of SS_V1 and SS_V2 by three figures of merit using viewing aspects 180 to 185° and elevation 0°.

Target	ϵ_W (unitless)	$\overline{\sigma}_W$ (dBm^2)	Weibull $_W$, $_W$ (m^2)
Vehicle Domain	0.07	4-18	0.6-1.0, 3-60
HellyHensen	0.59	10	0.9, 10
NHTSA FC-1	0.52	16	1.1, 30
NHTSA FC-2	0.57	0	0.7, 1
NHTSA SS_V1	0.04	12	0.5,6
NHTSA SS_V2	0.03	16	0.4, 13

Figure of merit: Target Instability

The instability of target signatures measured pulse-to-pulse is plotted for various targets. The independent axis in Figures 72 and 73 is simply an index into MTRI's target database.

Table 7: Ka-band evaluation of SS_V1 and SS_V2 by three figures of merit using viewing aspects 180 to 185° and elevation 0°. Statistics are based on five vehicles, a subset of the twenty-five cars sampled at W-band.

Target	ϵ_K (unitless)	$\overline{\sigma}_K$ (dBm^2)	Weibull $_K$, $_K$ (m^2)
Vehicle Domain	0.02	13-16	0.9-1.3, 20-30
NHTSA SS_V1	0.004	18	0.6,30
NHTSA SS_V2	0.007	14	0.7,20

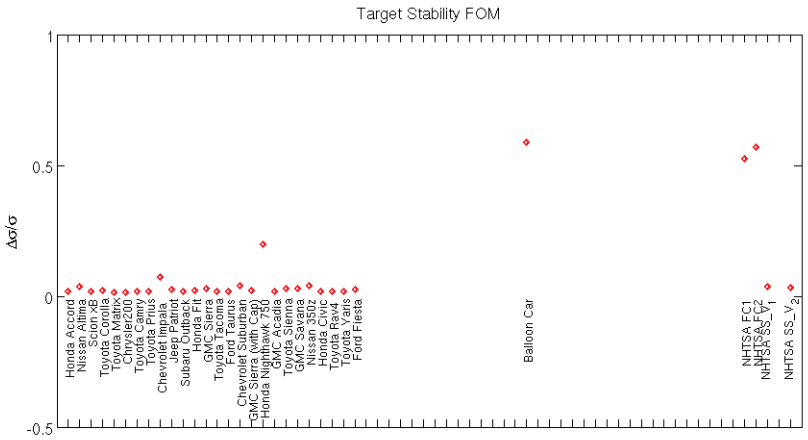

Figure 72: Instability metric of 26 vehicles and 5 surrogates at W-band.

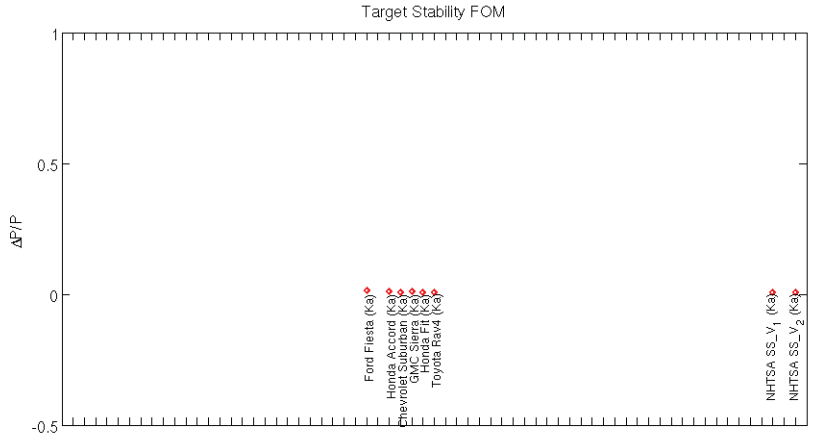

Figure 73: Instability metric of 6 vehicles and 2 surrogates at Ka-band.

Figure of merit: Expected RCS

The mean radar cross-section over the span of viewing angles and frequencies is plotted for various targets. The independent axis in Figures 74 is simply an index into MTRI's target database.

We've measured the target response with an elevated beam-pointing, in Figure 75, as well. Radar designers may opt to elevate the bore-sight of the antenna for a PCS system to reduce the return level from ground clutter. They may also wish to have multiple beams to better identify the height extent of objects in the radar's field of view. These values are not reflected in Tables 6 and 7, but are included here for completeness.

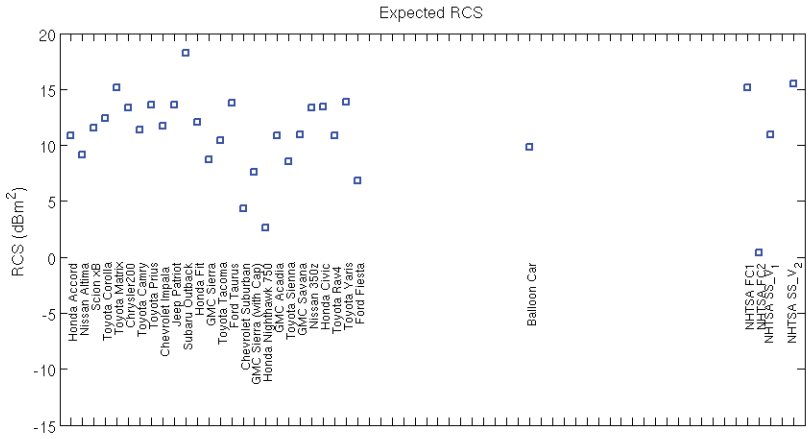

(a) W-band mean RCS at 0.0° elevation

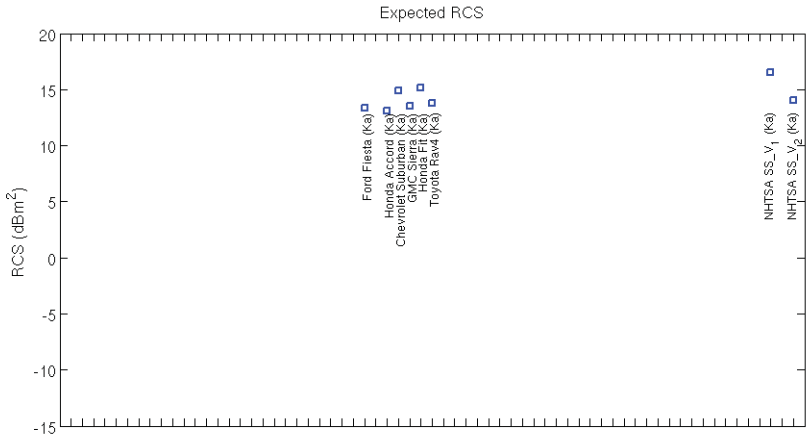

(b) Ka-band mean RCS at 0.0° elevation

Figure 74: (a) Mean W-band RCS of 26 vehicles and 5 surrogates measured at elevation of 0.0°. (b) Mean Ka-band RCS of 6 vehicles and 2 surrogates measured at elevation of 0.0°.

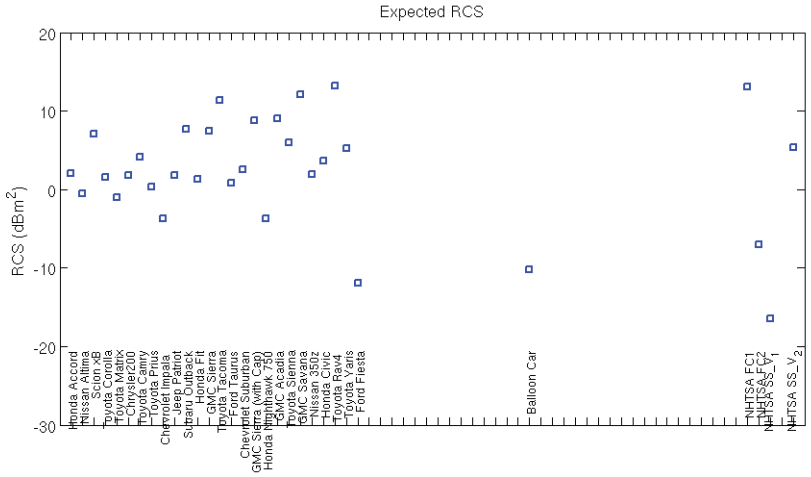

(a) W-band mean RCS at 1.5° elevation

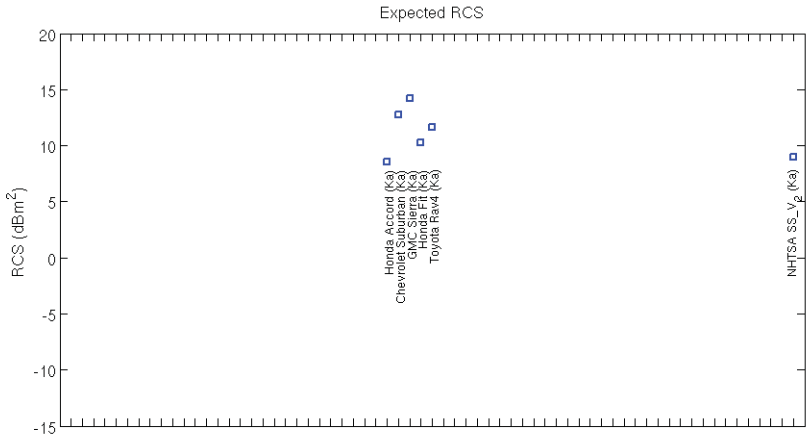

(b) Ka-band mean RCS at 1.5° elevation

Figure 75: (a) Mean W-band RCS of 26 vehicles and 5 surrogates measured at elevation of 1.5°. (b) Mean Ka-band RCS of 5 vehicles and 1 surrogate measured at elevation of 1.5°. Collections of the SS_V1 were collected with an elevation bias of 0.4° higher compared to measurements of the SS_V2 - resulting in low measured values for the SS_V1 at 1.5° elevation.

Figure of merit: Weibull Parameters

Probability density functions are formed from the histograms of measurements collected for each target. These PDFs are then fitted to a Weibull distribution by a Maximum-Likelihood Estimation (MLE) algorithm. The resulting plots help highlight that the physical shape of a target dominates the strength of its radar response, not its physical size. The compact cars typically have larger radar reflections than trucks. This is a result of the trucks having a fairly flat shape at the bumper, as opposed to contoured bumpers, rear-spoilers and fully-surrounded license plate shelters. While trucks have larger and sturdier suspension, it is not shaped to promote the vehicle's RCS at rear-aspect. In the case of SUVs, the combination of a high-suspension with a rounded back-end can create a RCS significantly lower than a compact vehicle with a lower-suspension and a bumper height that does not obscure so much of the chassis. These results have an interest to automotive PCS radar designers and vehicle safety test designers alike. The best-fit, Weibull parameter pairs are plotted in Figures 76 through 79.

We've measured the target response with an elevated beam-pointing, as well. These values are not reflected in Tables 6 and 7, but are included here for completeness.

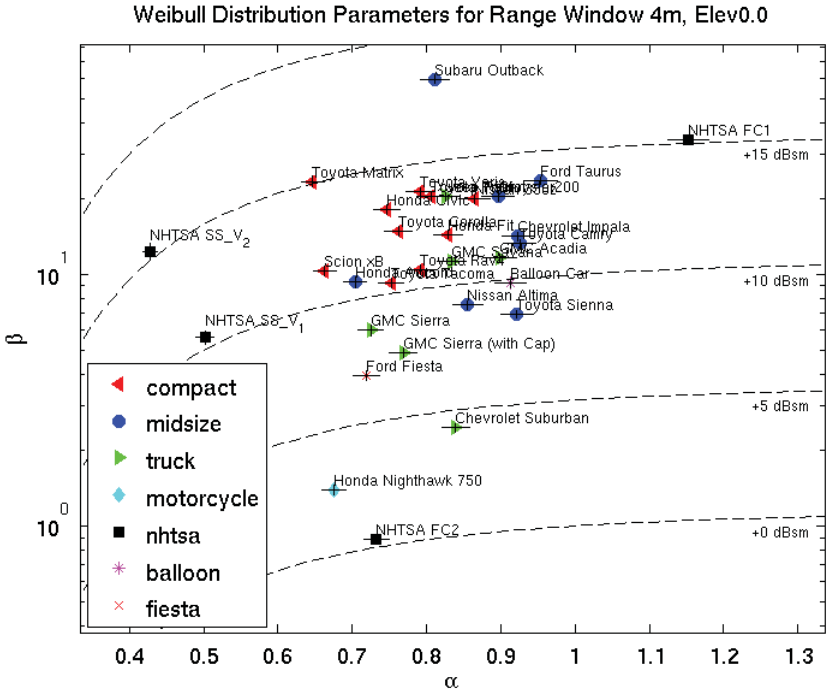

Figure 76: Weibull scale plotted against shape for 26 vehicles and 5 surrogates measured at W-band at elevation of 0.0°.

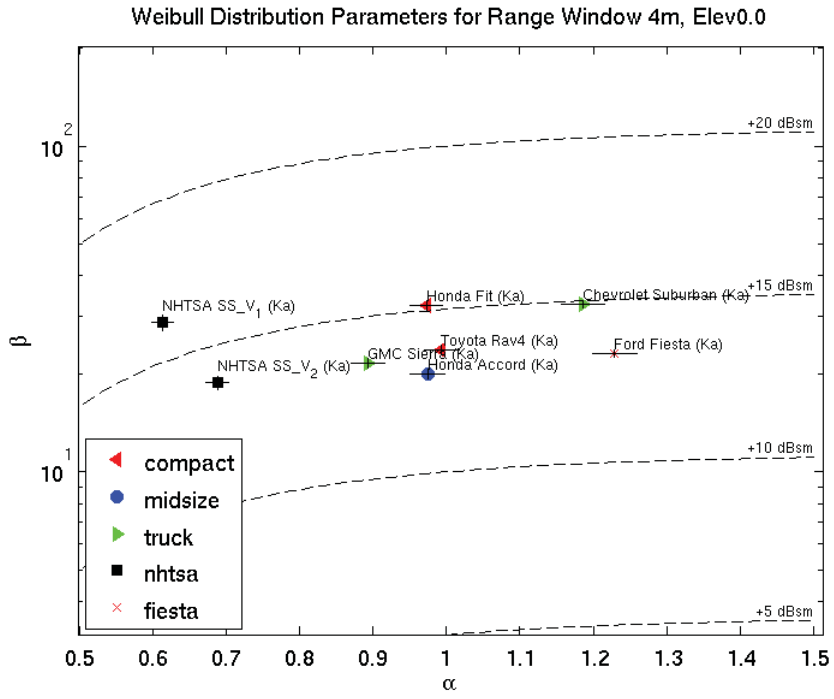

Figure 77: Weibull scale plotted against shape for 6 vehicles and 2 surrogates measured at Ka-band at elevation of 0.0°.

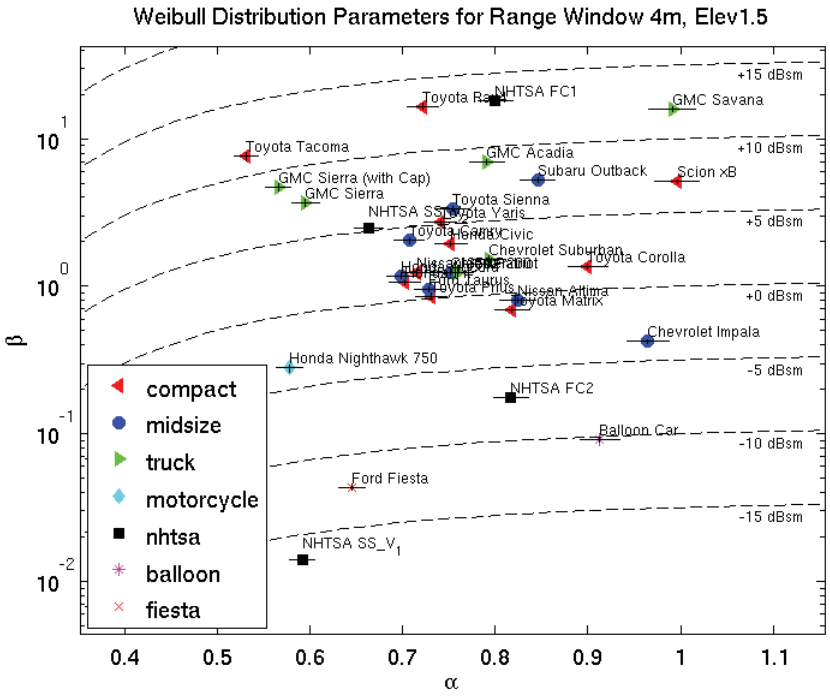

Figure 78: Weibull scale plotted against shape for 26 vehicles and 5 surrogates measured at W-band at elevation of 1.5°. Collections of the SS_V1 were collected with an elevation bias of 0.4° higher compared to measurements of the SS_V2 - resulting in low measured values for the SS_V1 at 1.5° elevation.

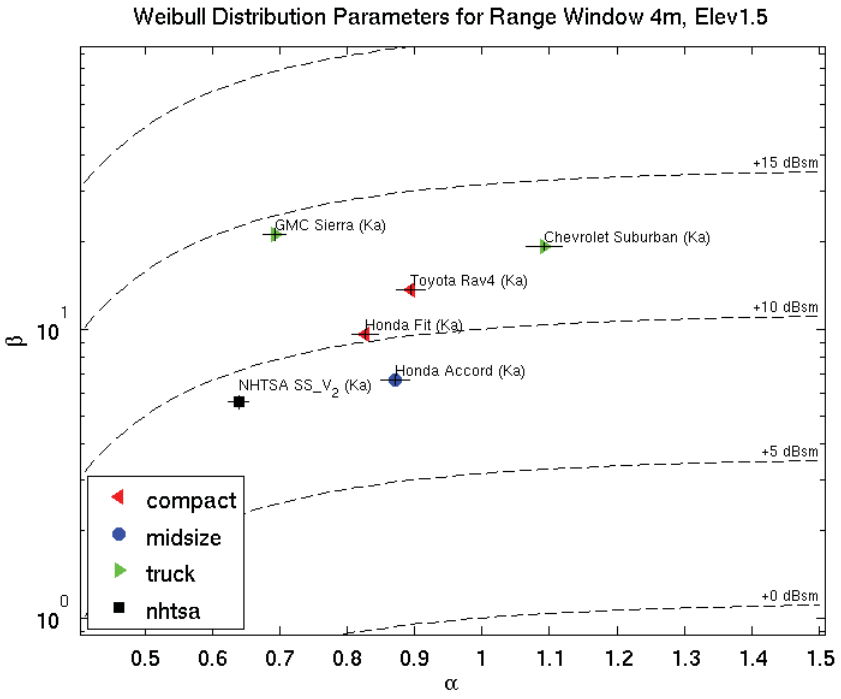

Figure 79: Weibull scale plotted against shape for 5 vehicles and 1 surrogates measured at Ka-band at elevation of 1.5°.

7.2 Evaluation of test surrogates at 180° viewing aspect angle

In this section, we closely parallel the material in Section 7.1, but restrict our analysis of the data collected at the viewing aspect of 180° to understand the reflectance of the SS_V surrogate for automotive tests with a vehicle approaching directly from behind. The figures of merit for all of the targets are tabulated for W-band in Table 8 and Ka-band in Table 9. These tables allow the reader to determine whether each surrogate is within the Vehicle Domain. The SS_V2 is the only surrogate to be within the Vehicle Domain. Technically, the SS_V2 presents too large a returns at Ka-band, $\overline{\sigma}_K$, is one dBm^2 above the maximum; however, there are only six vehicles in the Ka-band collection library and the margin of error for these collections is approximately 2 dB, based on the variance measured on the calibration target. Similarly, the value of $_K$ exceeds the maximum by a ratio of 1.25, less the 2 dB (ratio of 1.6) we estimate for measurement error.

Table 8: W-band evaluation of SS_V1 and SS_V2 by three figures of merit using the tail aspect, 180 °.

Target	ϵ_W (unitless)	$\overline{\sigma}_W$ (dBm^2)	Weibull $_W$, $_W$ (m^2)
Vehicle Domain	0.07	4-22	0.5-1.3, 2-160
HellyHensen	0.59	12	0.9, 16
NHTSA FC-1	0.52	17	1.3, 50
NHTSA FC-2	0.57	3	1.0, 2
NHTSA SS_V1	0.04	15	1.0, 32
NHTSA SS_V2	0.03	21	1.1, 126

Figure of merit: Expected RCS

Following analysis similar to that in Section 7.1, the mean radar cross-section at 180° aspect is plotted for various targets in Figure 80. The independent axis is simply an index into MTRI's target library.

We've measured the target response with an elevated beam-pointing, as well. Radar designers may opt to elevate the bore-sight of the antenna for a PCS system to reduce the return level from ground clutter. They may also wish to have multiple beams to better identify the height extent of objects

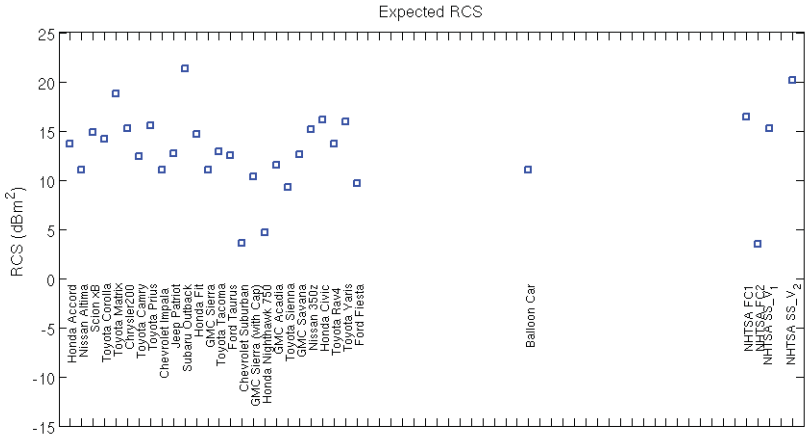

(a) W-band mean RCS at 0.0° elevation

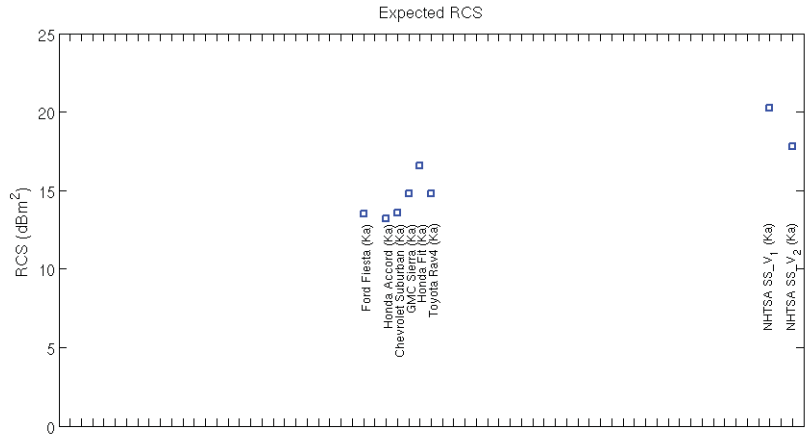

(b) Ka-band mean RCS at 0.0° elevation

Figure 80: (a) Mean W-band RCS of 26 vehicles and 5 surrogates measured at aspect 180.0° and elevation of 0.0°. (b) Mean Ka-band RCS of 6 vehicles and 2 surrogates measured at aspect 180.0° and elevation of 0.0°.

Table 9: Ka-band evaluation of SS_V1 and SS_V2 by three figures of merit using the tail aspect. Statistics are based on six vehicles, a subset of the twenty-six cars sampled at W-band.

Target	ϵ_K (unitless)	$\overline{\sigma}_K$ (dBm^2)	Weibull $_K$, $_K$ (m^2)
Vehicle Domain	0.02	13-17	1-1.2, 20-50
NHTSA SS_V1	0.004	21	1.0,126
NHTSA SS_V2	0.007	18	1.1, 63

in the radar's field of view. These values are not reflected in Tables 8 and 9, but are included here for completeness.

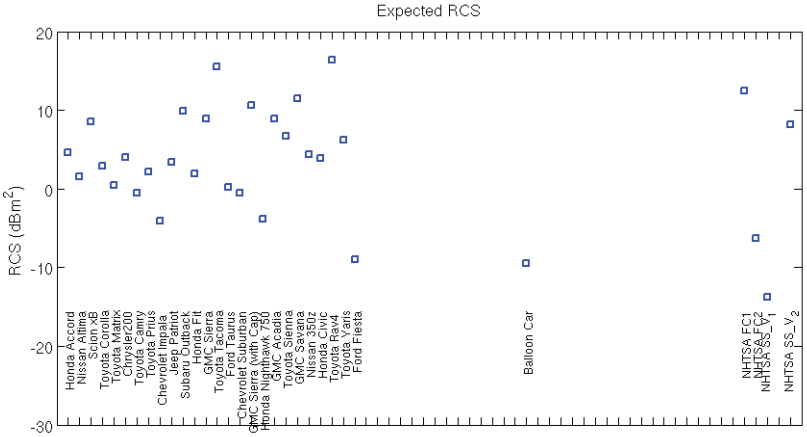

(a) W-band mean RCS at 1.5° elevation

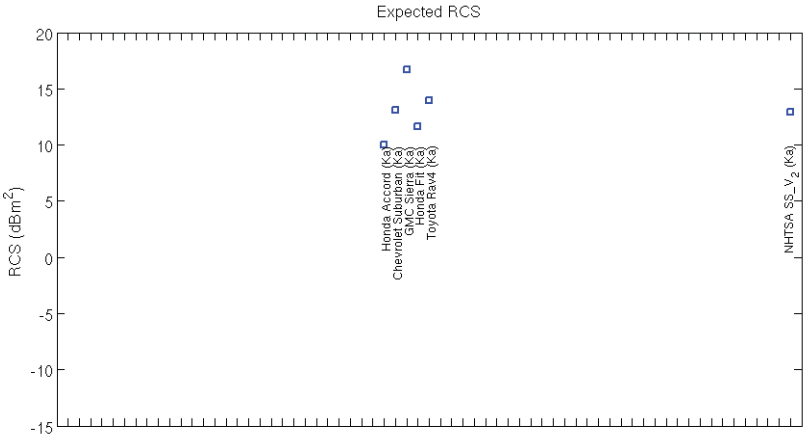

(b) Ka-band mean RCS at 1.5° elevation

Figure 81: (a) Mean W-band RCS of 26 vehicles and 5 surrogates measured at aspect 180.0° and elevation of 1.5°. (b) Mean Ka-band RCS of 5 vehicles and 1 surrogate measured at aspect 180.0° and elevation of 1.5°. Collections of the SS_V1 were collected with an elevation bias of 0.4° higher compared to measurements of the SS_V2 - resulting in low measured values for the SS_V1 at 1.5° elevation.

Figure of merit: Weibull Parameters

Following analysis similar to that in Section 7.1, probability density functions are formed from the histograms of measurements collected for each target, but using only data collected from directly behind the target, denoted as aspect 180° and elevation 0°.

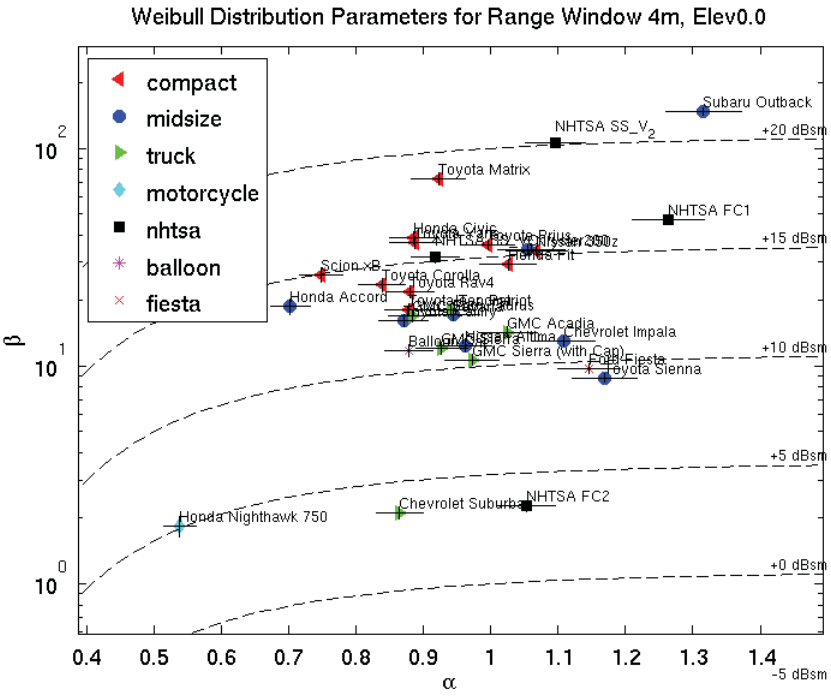

Figure 82: Weibull scale plotted against shape for 26 vehicles and 5 surrogates measured at W-band at elevation of 0.0°.

We've measured the target response with an elevated beam-pointing, as well. These values are not reflected in Tables 8 and 9, but are included here for completeness.

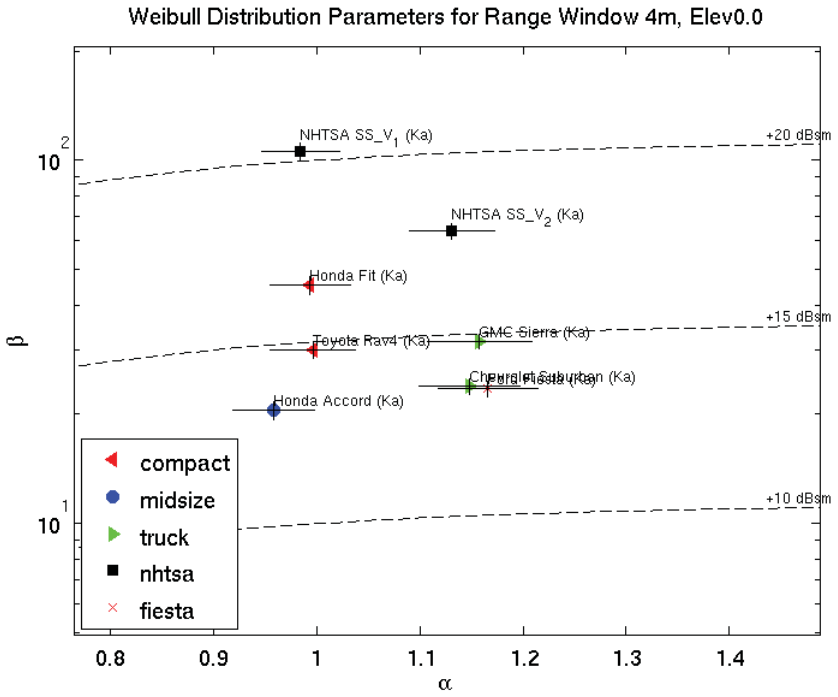

Figure 83: Weibull scale plotted against shape for 6 vehicles and 2 surrogates measured at Ka-band at elevation of 0.0°.

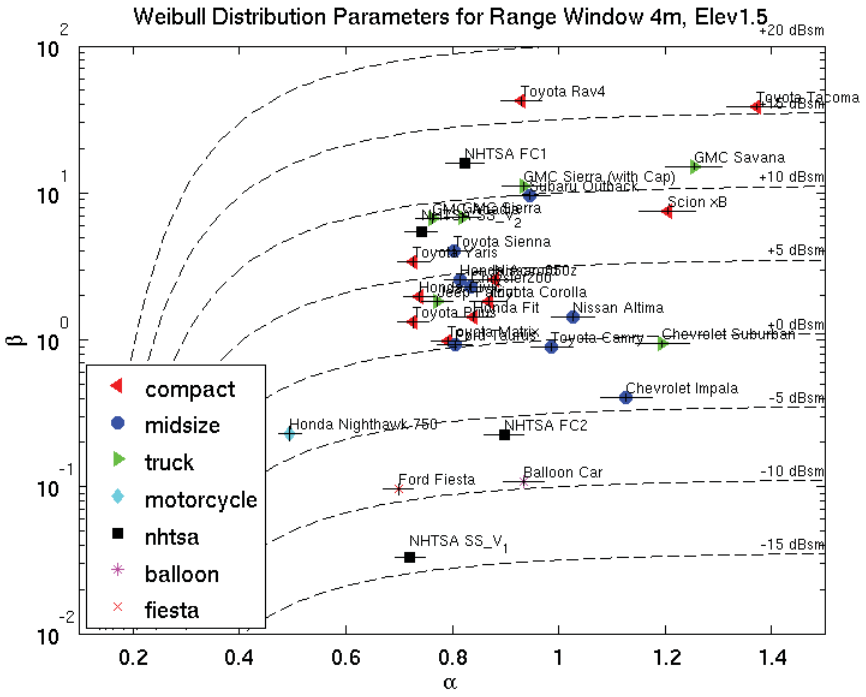

Figure 84: Weibull scale plotted against shape for 26 vehicles and 5 surrogates measured at W-band at elevation of 1.5°. Collections of the SS_V1 were collected with an elevation bias of 0.4° higher compared to measurements of the SS_V2 - resulting in low measured values for the SS_V1 at 1.5° elevation.

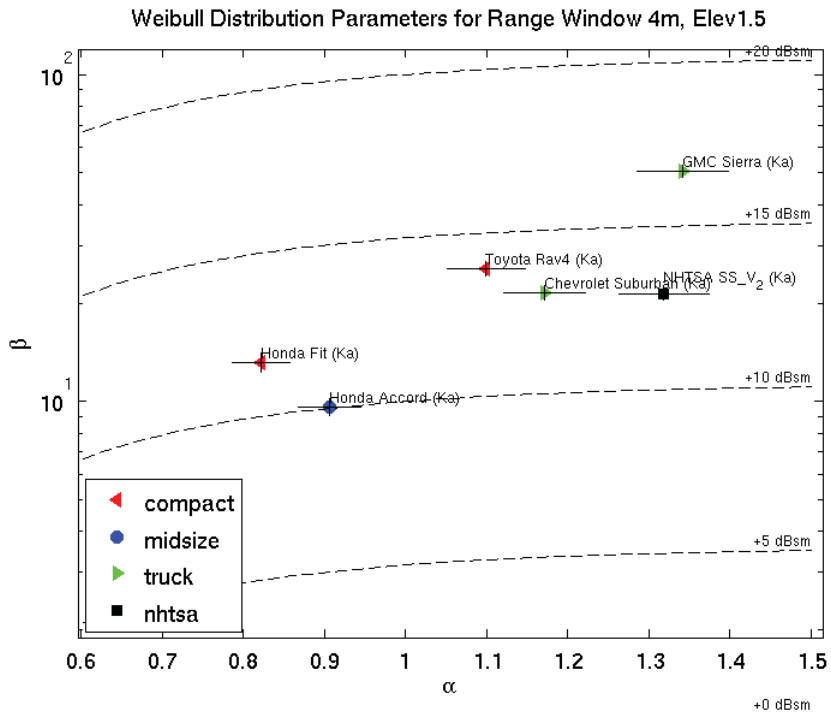

Figure 85: Weibull scale plotted against shape for 5 vehicles and 1 surrogate measured at Ka-band at elevation of 1.5°.

8 Discussion

8.1 Background

Automotive collision mitigation systems employ active optical, lidar and radar sensors to detect and track the location and dynamic states of other vehicles. In this report, we've analyzed results of radar measurements of the US-DOT/NHTSA SS_V test surrogates. These vehicle surrogates are designed for use in testing collision mitigation systems. To evaluate the quality of the surrogate, we have considered the impact of the surrogates radar reflectance on the functions of detection and tracking. Radar detection algorithms are tuned to minimize errors. In classical hypothesis testing approaches, we define Type I errors as false detections, or false alarms, and Type II errors as missed detections. Written more formally, Type I errors are the probability that a hypothesis test shows positive, H_1, exceeds the test threshold, τ, when the null-hypothesis, H_0, is true. And Type II errors are committed when the null-hypothesis exceeds the detector's threshold, although the condition warranting alarm is true.

$$TypeI : P(H_1 > \tau | H_0) \tag{12}$$

$$TypeII : P(H_0 > \tau | H_1) \tag{13}$$

A graphic example, for clarity, is shown in Figure 86. By varying the threshold and evaluating the Type I and Type II error rates, we can evaluate the detection error trade-offs for the target and clutter, assuming a simple threshold detector.

Weighing the cost of each error is the job of the system designers, but it is important to note that the selection of optimal detection thresholds is predicated on the statistical distribution of targets of interest, other targets (clutter) and the inherent system noise.

Additional considerations that impact the systems ability to detect and track targets of interest is how the measurements are drawn from the distribution. That is, how the measurement changes each time the radar performs a measurement: Does it change quickly, or slowly. For this case, we consider whether the signature changes with respect to the radar's viewing aspect of the target (slowly), or does it change with repeated measurement from the same viewing aspect (quickly).

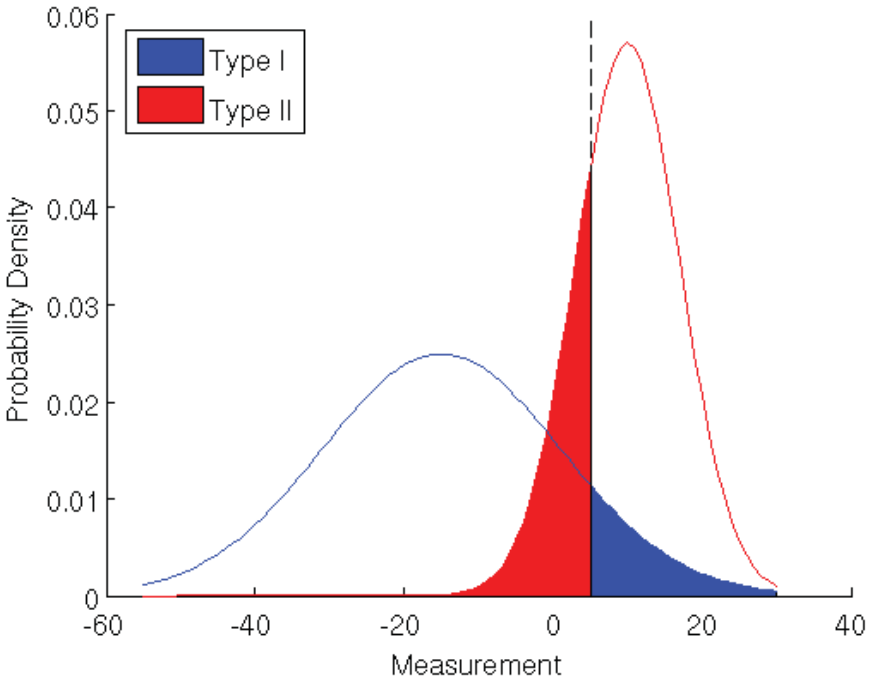

Figure 86: The red-curve is the target of interest, the blue-curve is for targets not of interest and the black dashed-line is the threshold. Type I and Type II errors are shown. It is important to note that Type I and Type II errors depend on the statistical distribution of the targets of interest and targets not of interest, as well as the choice of threshold.

8.2 Summary Results

What is found in the analysis of 26 vehicles at W-band and 6 vehicles at Ka-band is that there is a large variety of signatures. Both the SS_V1 and SS_V2 provide a reflectance with reasonable average reflected power, though their distributions have greater variation than most vehicles (this is manifest in the slightly low shape value assessed over the 5° of azimuth). From field analysis and engineering judgement, this is likely due to the large flat strike area of the SS-V, which is a design element that permits the surrogate to absorb the large amount of kinetic energy required during tests. The SS1 had an average RCS value measured at Ka-band that exceeded the values of typical cars. This was corrected through modifications in the design of SS_V2, which has an expected RCS similar to our sample of vehicles. As at W-band, the response at Ka-band of the SS_V1 and SS_V2 shows that the distribution of the targets' response exhibits greater variation than a typical vehicle.

8.3 Performance Estimates for Automotive Safety Tests

Restricting our attention to the tail aspect case, we estimate the error trade-off for a classical threshold detector. Using the road returns measured during our collections we can consider the detector error trade-off (DET) plot [9]. This allows us to see how the error rates associated with the Weibull distribution of the SS_V2 compares with the error rates expected for a Weibull distribution using the Nominal Vehicle shape and scale. The *Nominal Vehicle* parameters are chosen by estimating the center of the domain formed by all of the vehicles, as in Figure 82 in Section 7.2. That is, by visual inspection of the Weibull parameters of all the vehicles, we are estimating the mean shape parameter, , and the log geometric-mean of the scale, , and defining this as a Nominal Vehicle. Weibull shape and scale parameters for the SS_V2, the Road and the Nominal Vehicle listed in Table 10.

Comparing the error trade-offs for a threshold test using the Weibull parameters for the SS_V2 and the Nominal Vehicle with road as the clutter, the results, which are plotted in Figure 87 show that the SS_V2 should incur errors at a lower rate than the Nominal Vehicle.

We can also relax the constraint on angle and use the results from the full 5° collection window and find the situation is reversed. Over the 5° collection window, the SS_V2 has smaller returns at the off-tail aspect and the detector

Table 10: Weibull parameters, (unitless), and (m^2), for the SS_V2 and a Nominal Vehicle assessed at tail aspect. Road measurements are used as clutter. These parameters are used to estimate the detector errors.

Band	SS_V2	Nominal Vehicle	Road
W	1.1, 126	1, 20	0.7, 0.0016
Ka	1.1, 63	1.1, 30	0.5, 0.0006

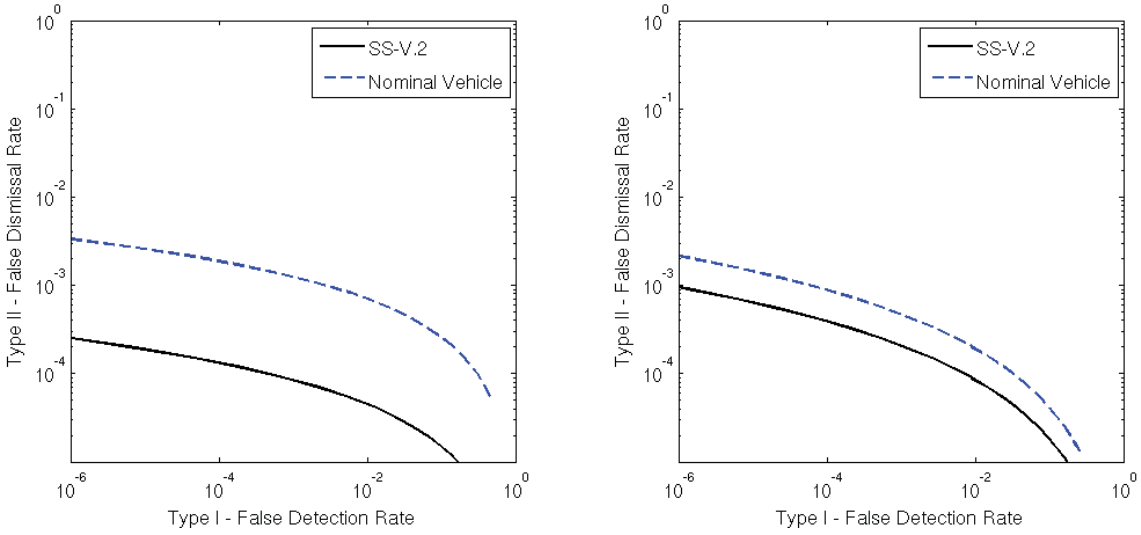

(a) W-band errors.

(b) Ka-band errors.

Figure 87: Comparison of errors expected for detection of the SS_V2 and a Nominal Vehicle in road conditions when viewing is restricted to tail aspect.

suffers more errors than the Nominal Vehicle, as can be seen in Figure 88.

Table 11: Weibull parameters, (unitless), and (m^2), for the SS_V2 and Nominal Vehicle assessed over 5° collection window. Road measurements are used as clutter. These parameters are used to estimate the detector errors.

Band	SS_V2	Nominal Vehicle	Road
W	0.4, 13	0.8, 10	0.7, 0.0016
Ka	0.7,20	1, 15	0.5, 0.0006

These results show that compared to the Nominal Vehicle from our library of vehicles, performance estimated with the NHTSA SS_V2 should be *optimistic* in the case of a tail-on approach, at 180°, by the striking vehicle, becoming *pessimistic* as the approach angle varies. This evaluation considers the radar response of the target and its impact on the probability of detection. The terms *optimistic* and *pessimistic* refer to the target detectability.

This evaluation is good for comparing the relative detectability of the SS_V2 and a set of Weibull parameters chosen as a Nominal Vehicle. This evaluation does not characterize the performance of any collision mitigation system, as the sampling of each vehicle is sparse and the performance of any detection system will be determined by the details of its implementation.

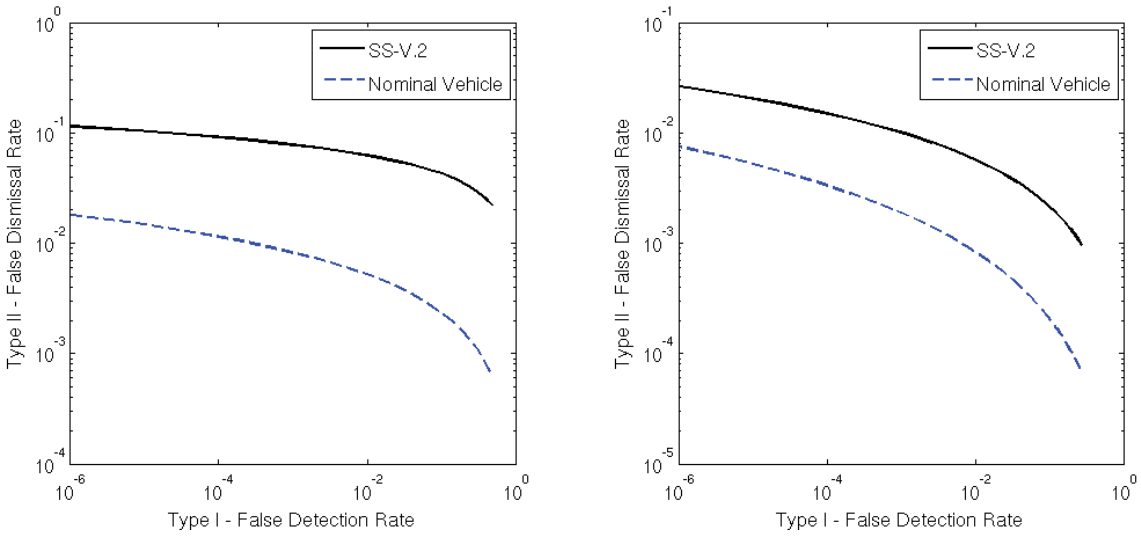

(a) W-band errors.

(b) Ka-band errors.

Figure 88: Comparison of errors expected for detection of the SS_V2 and a Nominal Vehicle in road conditions when viewing is covers upto 5° near tail-aspect.

8.4 Conclusions

We conclude that the SS_V2 is a viable surrogate for automotive safety tests where the vehicle under test approaches the stationary target from the tail-aspect. Under these conditions the SS_V2 will provide an optimistic estimate of performance for the vehicle under test against the Nominal Vehicle defined in this research for analysis and is within the parametric bounds of the vehicles sampled to date. It is obvious, but bears repeating that actual vehicles also vary from the Nominal Vehicle. Indeed, this is a consideration that merits further analysis. Currently, the SS_V2 provides a realistic target for evaluating the performance of a vehicle under test, with regard to the target's response at W or Ka-band. However, such a test does not provide information on how the performance of the vehicle under test degrades with more *pessimistic* targets. Analysis of the error trade-offs for the vehicle data collected in this study can be used to understand the critical target models for evaluating the response of vehicles in automotive safety tests.

References

[1] K. Kusano and H. Gabler, "Identification of target populations for current active safety systems using driver behavior," in *IEEE Intelligent Vehicles Symposium, Proceedings*, 2012, pp. 655–660.

[2] NHTSA, *National Automotive Sampling System (NASS) General Estimates System (GES).* U.S. Dept. of Trans., NHTSA, 2009.

[3] G. Forkenbrock and F. Barickman, "Forward collision warning (fcw) performance evaluation," in *21st Enhanced Safety Vehicles Conference*, Stuttgart, Germany, 2009, pp. Paper No. 09–0561.

[4] F. Weinmann, "Frequency dependent rcs of a generic airborne target," in *URSI EMTS International Symposium on Electromagnetic Theory*, Berlin, Germany, 2010, pp. 977–980.

[5] W. Buller, B. Wilson, L. van Nieuwstadt, and J. Ebling, "Statistical modeling of measured automotive radar reflections," in *Proceedings, IEEE International Instrumentation and Measurement Technology Conference, submitted*, 2013.

[6] E. F. Knott, *Radar Cross Section Measurements.* Raleigh, North Carolina: SciTech Publishing Inc., 2006.

[7] R. Gilbert, P. Zoratti, R. Becker, G. Brumbaugh, T. Chaplin, M. Harrison, M. Hawks, and K. Gondoly, *Characterization and Evaluation of a Prototype Forward-Looking Automotive Radar Final Report.* Ann Arbor, Michigan: Environmental Research Institute of Michigan (ERIM), 1997.

[8] P. Swerling, *Probability of Detection for Fluctuating Targets, RM-1217.* Santa Monica, California: Rand Corporation, 1954.

[9] A. Martin, G. Doddington, T. Kamm, M. Ordowski, and M. Przybocki, "The det curve in assessment of detection task performance," in *Proceedings of Eurospeech '97*, Rhodes, Greece, 1997, pp. 1895–1898.

DOT HS 811 817
August 2013

U.S. Department
of Transportation
**National Highway
Traffic Safety
Administration**

9784-080813-v2a